NASA
Technical
Paper
2443
C.2
March 1985

Effects of Chromium and Aluminum on Mechanical and Oxidation Properties of Iron-Nickel-Base Superalloys Based on CG-27

Susan R. Schuon

NASA

NASA
Technical
Paper
2443

1985

Effects of Chromium and Aluminum on Mechanical and Oxidation Properties of Iron-Nickel-Base Superalloys Based on CG-27

Susan R. Schuon

Lewis Research Center
Cleveland, Ohio

NASA
National Aeronautics
and Space Administration

Scientific and Technical
Information Branch

Summary

One of the objectives of the NASA Conservation of Strategic Aerospace Materials Program is to provide an understanding of the role of chromium in iron-nickel-base aerospace alloys. The effects of chromium and aluminum on the mechanical and oxidation properties of a test matrix of gamma-prime-strengthened alloys based on CG-27 were studied. CG-27 is a high-strength iron-nickel-base alloy for use at intermediate temperatures (650 to 870 °C). The alloy test matrix was based on the reduction of Cr from 12 to 8 to 4 to 0 wt %. Aluminum was increased from 1.5 to 3 to 6 wt %. Cast alloys were studied in order to isolate compositional effects. Alloys were tested in tension at room temperature and 760 °C and stress-rupture tested at 760 °C under stresses of 172 and 276 MPa. Alloys were oxidized for 200 1-hr cycles at 870 °C.

Based on the following observations, a reduction in chromium to 4 wt % was possible if the aluminum content was increased to 3 wt %: The stress-rupture life of the alloys reached a maximum at 4 wt % Cr and 3 wt % Al and then dropped at higher levels of Cr and Al. Since gamma-prime coherence had little effect on strength, gamma-prime dispersion and solid-solution strengthening were the principal modes of alloy strengthening. The oxidation attack parameter K_a decreased with higher Cr and Al content, that is, oxidation resistance improved. As a group, alloys with 3 wt % Al had the lowest attack parameters. Therefore 3 wt % is the optimum level of Al for parabolic oxidation behavior. Spalling, due to diffusion-induced grain growth, was controlled by the overall Cr and Al levels.

The alloy NCG-7 (4 wt % Cr and 3 wt % Al) had stress-rupture properties superior to those of the base alloy, CG-27, and maintained parabolic oxidation behavior while the Cr content was reduced by 67 percent.

Introduction

Since the advent of high-strength nickel-base superalloys, little research has concentrated on iron-base superalloys. However, they have lower strategic material content and cost, as well as good mechanical properties at intermediate temperatures (ref. 1). Gamma-prime-strengthened iron alloys have found use in gas turbine engines as blades, disks, casings, and fasteners. They also have potential in automotive gas turbine (ref. 2) and Stirling engines (ref. 3).

The role of chromium in iron-base superalloys has been studied as part of the NASA Conservation of Strategic Aerospace Materials Program. Although the tonnage of chromium used in the aerospace industry is comparatively small, chromium is absolutely essential for oxidation and corrosion resistance. Since major U.S. sources of chromium are in countries from which supplies may be disrupted, alternative metals are sought. The alternatives to chromium for oxidation resistance are silicon and aluminum. Silicon is undesirable because of its tendency to enhance the formation of sigma phase and an oxide that is unprotective at higher temperatures. Aluminum forms a desirable oxide, but stress-rupture properties are adversely affected at higher levels of aluminum. Most commercial alloys have more than 12 wt % Cr and less than 1.5 wt % Al.

The purpose of this study was twofold: first, to determine if Cr can be reduced in CG-27, a promising gamma-prime-strengthened iron alloy, while its mechanical and oxidation properties are maintained or improved and, second, to gain a better understanding of the role of chromium and aluminum in mechanical and oxidation behavior.

Experimental Procedure

Materials and Fabrication

Cast alloys based on CG-27, an alloy normally used in the wrought condition, were evaluated for mechanical properties and oxidation resistance. The series of alloys (shown in table I) was based on the nominal reduction of Cr from 12 to 8 to 4 to 0 wt % in CG-27. NCG-1 represents the cast version of CG-27. Aluminum was nominally increased from 1.5 to 3 to 6 wt %. Pure elements were added to 1018 steel. The alloys were melted in zirconia crucibles and cast into test bars. In some cases, zirconium pickup from the crucibles was substantial, as shown in table I. After casting, the alloys were solution treated in a vacuum for 1 hr at 1038 °C and aged for 16 hr at 760 °C. Tensile and stress-rupture bars were tested in the heat-treated condition. Oxidation test

TABLE I.—CHEMICAL ANALYSES OF CAST ALLOYS

Alloy	Composition, wt %											%
	Fe	Ni	Cr	Al	Ti	Mo	Nb	Zr	P	C	S	Ferrite
NCG-1	39.8	37.0	12.4	1.7	2.6	5.7	0.67	0.011	0.013	0.10	0.011	0.2
NCG-2	44.4	37.4	7.5	1.7	2.5	5.6	.68	.044	.014	.13	.012	.4
NCG-3	48.6	37.5	3.6	1.4	2.5	5.6	.67	.021	.007	.12	.012	1.2
NCG-4	52.7	36.7	0	1.6	2.7	5.5	.65	.021	.015	.12	.012	9.0
NCG-5	37.3	38.5	12.8	2.8	1.9	5.8	.70	.038	.005	.11	.010	.2
NCG-6	43.4	37.6	7.4	2.8	2.1	5.7	.71	.19	.01	.12	.011	.5
NCG-7	48.2	36.5	3.5	3.1	2.3	5.6	.67	.18	.01	.11	.011	.2
NCG-8	52.6	36.2	0	3.0	2.7	5.2	.60	.01	.009	.11	.011	.4
NCG-9	32.4	40.2	12.5	4.9	2.1	6.0	.72	.43	.009	.13	.008	.4
NCG-10	35.8	42.2	7.5	5.2	2.2	5.9	.72	.43	.009	.13	.008	2.4
NCG-11	42.9	39.0	3.5	5.7	2.6	5.8	.72	.037	.01	.100	.007	.6
NCG-12	45.7	39.3	0	5.8	2.6	5.8	.68	.013	.009	.076	.006	4.2
CG-27[a]	39.1	38.0	13.0	1.5	2.5	5.0	.60	----	----	.12	----	----

Alloy	Composition, at %										
	Fe	Ni	Cr	Al	Ti	Mo	Nb	Zr	P	C	S
NCG-1	43.8	35.5	13.4	3.6	3.1	3.3	0.41	0.007	0.024	0.47	0.02
NCG-2	48.5	36.0	8.2	3.6	2.9	3.3	.41	.027	.026	.61	
NCG-3	52.5	36.3	3.9	3.0	3.0	3.3	.41	.013	.013	.57	
NCG-4	57.0	35.5	0	3.4	3.2	3.3	.40	.013	.028	.57	
NCG-5	43.1	36.6	13.7	5.8	2.2	3.4	.42	.023	.009	.51	
NCG-6	49.3	35.8	8.0	5.8	2.5	3.3	.43	.110	.018	.56	
NCG-7	54.3	34.8	3.8	6.4	2.7	3.3	.40	.110	.018	.51	
NCG-8	58.4	34.5	0	6.2	3.1	3.0	.36	.006	.016	.51	
NCG-9	42.6	37.4	13.2	9.9	2.4	3.4	.42	.006	.016	.59	.01
NCG-10	45.9	39.4	7.9	10.5	2.5	3.3	.41	.253	.016	.58	.01
NCG-11	53.1	36.2	3.7	11.5	2.9	3.3	.42	.022	.016	.35	.01
NCG-12	44.7	36.5	0	11.7	2.9	3.4	.40	.008	.016	.35	.01
CG-27[a]	42.4	36.5	14.1	3.1	2.9	3.2	.36	----	----	.56	----

[a]Nominal composition of commercial alloy

coupons (1.2 by 2.5 cm) were cut from the remaining casting.

Differential Thermal Analysis

Differential thermal analysis (DTA) was performed on the 12 alloys. Critical points, shown in table II, were determined during heating and cooling. Samples were heated at a rate of 10 °C/min in He flowing at 20 ml/min.

Microscopy and Phase Analysis

After testing, alloys were examined by optical, scanning, and transmission electron microscopy. Representative samples from each of the 12 alloy castings were cut, mounted, and polished. Samples were immersion etched with a solution of 33 percent HCl, 33 percent HNO_3, 33 percent acetic acid, and 1 percent HF.

Scanning electron microscopy was used to document tensile fracture surfaces, oxide surfaces, and cross sections. Energy dispersive x-ray analysis was used to obtain a qualitative chemical analysis of the oxides.

For transmission electron microscopy, 3-mm disks were electropolished with a twin-jet polishing unit. The electrolytic solution was 1:4.5:4.5 perchloric acid, acetic acid, and butylcellusolve.

Volume fraction gamma prime was determined by extraction, surface-replica, and thin-foil methods in order to cross-correlate answers. This was necessary because the extremely fine, uniform size of the gamma prime made methods of volume fraction determination difficult. Gamma prime was extracted from the matrix by an electrolytic solution of 1 percent citric acid and 1 percent ammonium sulfate in distilled water at a current density of 0.075 A/cm^2.

Mechanical Property Testing

The 12 alloys were tensile tested at room temperature and 760 °C. They were stress-rupture tested at stresses of 172 and 276 MPa at 760 °C. Creep rates were estimated

TABLE II.—DIFFERENTIAL THERMAL ANALYSIS OF EXPERIMENTAL ALLOY MODIFICATIONS

[All samples heated at 10 °C/min in He flowing at 200 ml/min.]

Sample	Sample heating		Sample cooling	
	γ' precipitation temperature, °C	Melting range, °C	Solidification range, °C	γ' precipitation temperature, °C
NCG-1	774-948	1260-1367	1350-1200	884-689
NCG-2	750-907	1250-1372	1355-1250	875-721
NCG-3	750-910	1298-1377	1368-1260	869-730
NCG-4	616-913	1302-1386	1370-1250	879-635
NCG-5	659-1030	1250-1344	1330-1170	915-750
NCG-6	750-928	1202-1320	1300-1155	817-782
NCG-7	769-920	1342-1362	1349-1178	890-743
NCG-8	620-980	1215-1318	1300-1160	885-805
NCG-9	725-910	1270-1370	1355-1193	870-735
NCG-10	629-889	1248-1345	1330-1137	892-768
NCG-11	749-900	1303-1390	1380-1250	869-652
NCG-12	620-910	1250-1355	1342-1180	880-750

from dial readings by determining the change in extension of the test specimen.

Oxidation Testing

Cyclic oxidation testing and, to a more limited extent, isothermal oxidation testing were performed on the matrix of alloy modifications. The entire matrix of alloys was tested for 200 1-hr cycles in static air at 870 °C. After evaluation, three representative compositions, NCG-1, NCG-3, and NCG-7, were held in a furnace in air at 870 °C for 0.5 and 20 hr in order to evaluate the growth of the oxide scales.

Cyclic oxidation was chosen to more closely simulate a realistic engine operating condition of continual heating and cooling. A description of the cyclic oxidation test rig is given by Barrett and Lowell (ref. 4). Alloy coupons were heated in static air for 1 hr at 870 °C. This heating cycle was followed by cooling to room temperature for 20 min. The temperature of 870 °C was chosen in order to accelerate environmental damage. Duplicate alloy coupons were treated and weighed after 1, 15, 30, 45, 60, 75, 90, 100, 115, 130, 145, 160, 175, 190, and 200 cycles to generate curves of weight loss as a function of time.

Weight-loss—time curves for iron-nickel alloys tend to have three shapes: parabolic, linear, and mixed behavior. Data were fitted to the general equation

$$\frac{\Delta w}{A} = k_1^{1/2} t^{1/2} - k_2 t \pm SEE \tag{1}$$

where Δw is the change in weight, t is time, A is the surface area of the specimen, k_1 and k_2 are oxidation constants, and SEE is the standard error of estimate. The constants k_1 and k_2 were derived when time—weight-loss data were fitted to equation (1). An oxidation attack parameter K_a can be defined as

$$K_a = (k_1^{1/2} + 10k_2) \tag{2}$$

If spalling predominates, the attack parameter is defined as

$$K_a = 20k_2 t \tag{3}$$

Postoxidation analysis included scanning electron and optical microscopy, energy-dispersive x-ray analysis, and x-ray diffraction of the oxides. Alloy coupons were examined on the oxide surface and in cross section.

Results and Discussion

Differential Thermal Analysis

Differential thermal analysis was performed on the alloy series to determine an appropriate heat-treatment schedule. The results are shown in table II. The differences in the critical points between heating and cooling reflect the effects of superheating and supercooling. The uncorrected range of the upper gamma-prime loop boundary for the series ranged from 817 to 948 °C. The standard heat treatment temperature for CG-27 of 1038 °C (for 1 hr) (ref. 5) guaranteed the dissolution of the gamma prime. This temperature is at least 100 °C below the solidus. The standard precipitation temperature of 760 °C (for 16 hr) (ref. 5) is just above the lower gamma-prime loop boundary of the series

of alloys. The critical points for the series are plotted against Al content and Cr content in figures 1 and 2, respectively. In figure 1, there is a dip of about 50 °C in the liquidus and solidus temperatures to 6 at % Al. There is an increase of about 20 °C in the gamma-prime solvi to 6 at % Al. In figure 2, the critical temperatures are plotted against at % Cr. There is a rise in the liquidus and solidus temperatures from 0 at % Cr to 4 at % Cr followed by a 50 °C drop in temperature to 8 at % Cr. In contrast, the gamma-prime loop remains almost constant regardless of at % Cr.

Microstructure

Representative heat-treated microstructures are shown in figure 3. There appear to be few differences due to the change in Cr and Al in the alloy matrix. The matrix of the alloys consisted of austenite with very little ferrite, as shown in table I. As shown by x-ray diffraction, the lattice spacing of the austenite increased from 0.3599 to 0.3610 nm as Al content increased from 1.5 to 6.0 wt %. Grain-boundary niobium carbides, determined by energy-dispersive x-ray spectroscopy, were present in both the cast and heat-treated microstructure. Alloys NCG-6, NCG-8, NCG-10, and NCG-12 had an acicular beta phase, as shown in figure 3(b). The beta phase was

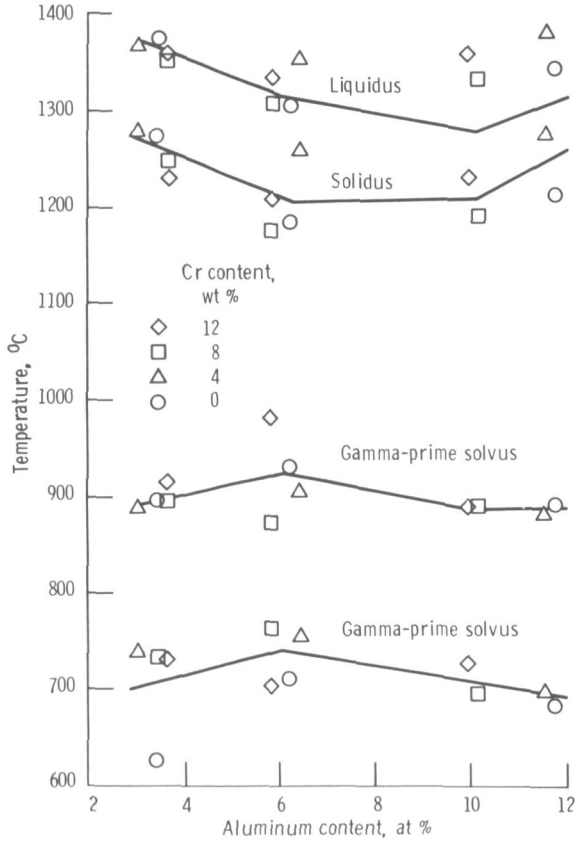

Figure 1.—Effect of aluminum content on critical temperatures in modified CG-27 alloys.

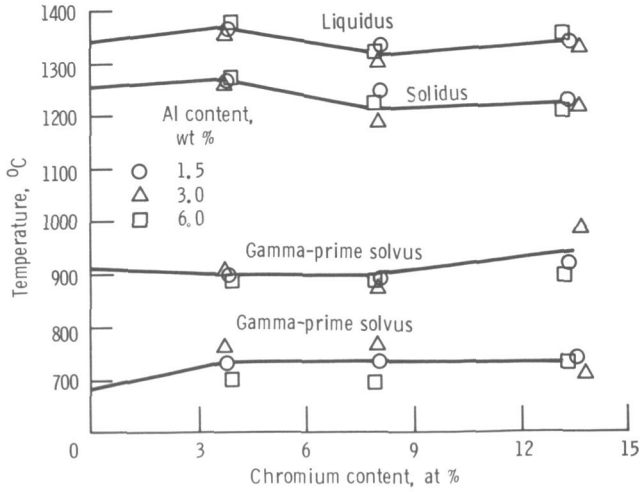

Figure 2.—Effect of chromium content on critical temperatures in modified CG-27 alloys.

determined by x-ray diffraction. A beta phase (Ni (Al Ti)) has been observed in a number of gamma-prime-strengthened iron-base superalloys. When the aluminum-titanium ratio is greater than 1, there is a tendency for the beta phase to form (ref. 6).

The principal strengthening phase in the matrix of the alloys was gamma prime, as shown in figure 4. Strengthening was due to gamma-prime precipitate size and volume fraction (refs. 6 and 7). The gamma-prime phase had a uniformly fine precipitate size. The average size of the gamma-prime particles ranged from 0.006 to 0.06 μm. The optimum size of gamma prime for strengthening ranges from 0.001 to 0.05 μm (ref. 6). As the ratio of Al to Ti increased, the gamma-prime shape changed from a mixture of squares and spheres to spheres.

The gamma prime was either incoherent (figs. 4(a) and (b)) or coherent (figs. 4(c) and (d)). When the thin foil is tilted 5° for NCG-4, the contrast of the gamma-prime particles changes. This indicates that the particles are incoherent with the matrix. While a majority of the alloy modifications had coherent gamma prime, NCG-3 and NCG-4 had incoherent gamma prime.

Most nickel-base alloys precipitate coherent gamma prime. However, incoherent gamma prime has been observed in some iron-nickel alloys such as IN901 (refs. 8 to 10). IN901 has a wt % composition of Fe-42Ni-12Cr-6Mo-3.22Ti-0.26Al. It has been proposed that incoherent gamma prime is heterogeneously nucleated on vacancy disks. Kuhlmann-Wilsdorf (ref. 11) found that the number of gamma-prime particles in IN901 was consistent with the predicted density of vacancy disks expected from heat treatment. As may be seen in figure 4(e), gamma-prime particles pinned dislocations, which confirmed the role of gamma prime in strengthening the alloy. The presence of incoherent gamma prime indicates

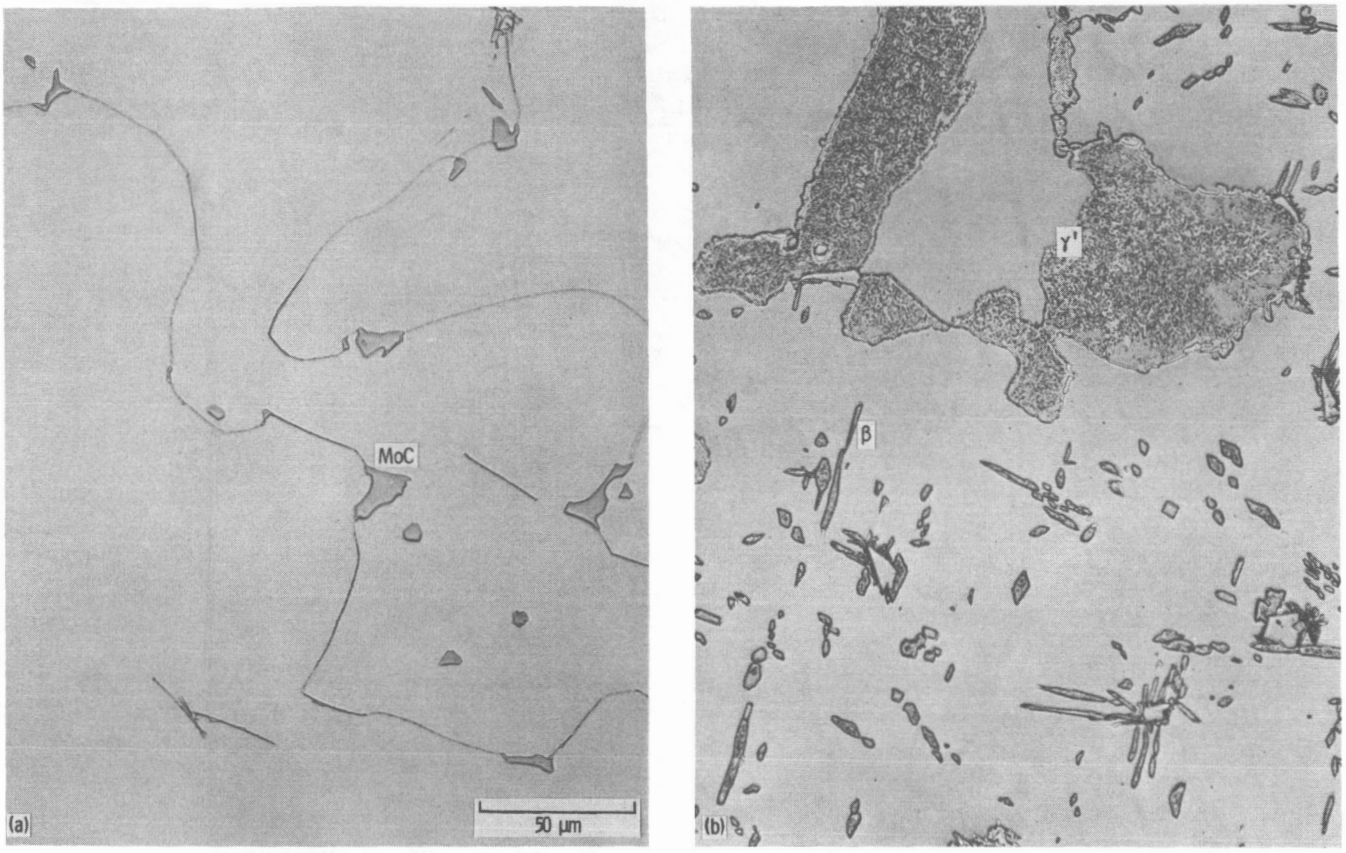

(a) NCG-2, 8 wt % Cr and 1.5 wt % Al, showing austenite and carbide phases.
(b) NCG-12, 0 wt % Cr and 6 wt % Al, showing austenite, gamma-prime, and beta phase.

Figure 3.—Representative optical micrographs of heat-treated, modified composition CG-27 alloys.

that the primary role of gamma prime was in dispersion strengthening rather than in coherency strains.

The volume fraction of gamma prime was determined by phase extraction, thin-foil microscopy, and TEM replicas. The volume fraction of gamma prime ranged from 7.8 to 11.5 vol % by phase extraction and thin-foil microscopy. However, there was considerable scatter in the data and no pattern consistent with composition. By TEM replica, the volume fraction of gamma prime ranged from about 8 vol % for 1.5 wt % Al alloys to about 6 vol % for 3 wt % Al alloys and was about 5 vol % for 6.0 wt % Al alloys. The reduction in volume fraction of gamma prime with increasing Al could be due to the precipitation of beta phase with increasing Al/Ti. The formation of a sigma phase is a concern in any iron-nickel-base superalloy. No sigma phase was observed in these alloys.

Mechanical Properties

Table III presents tensile and stress-rupture properties of the matrix of alloys determined at room temperature and 760 °C.

Tensile strength.—The room-temperature yield strength ranged from 601 MPa for NCG-1 (12 wt % Cr and 1.5 wt % Al) to 889 MPa for NCG-12 (0 wt % Cr and 6 wt % Al), as shown in table III(a). In general, the Cr content had little effect on the yield strength of the alloys both at room temperature and at 760 °C (tables III(a) and (b)). One exception was at 6 wt % Al, where the yield strength was proportional to a decrease in Cr content at room temperature. This effect was not observed at 760 °C. Yield strength was proportional to an increase in aluminum content at room temperature. However, aluminum content had little effect on the yield strength at 760 °C. The 3 wt % Al alloys had only a slightly higher yield strength than the 1.5 wt % Al or 6 wt % Al alloys.

The room-temperature ultimate tensile strength (table III(c)) ranged from 889 MPa for NCG-12 (0 wt % Cr and 6 wt % Al) to 643 MPa for NCG-8 (0 wt % Cr and 3 wt % Al). The Cr content had little effect on the ultimate tensile strength for alloys with 1.5 wt % Al and 6 wt % Al at room temperature. Alloys with 3 wt % Al had a lower ultimate tensile strength than either group of alloys with 1.5 wt % or 6 wt % Al. At 760 °C, the

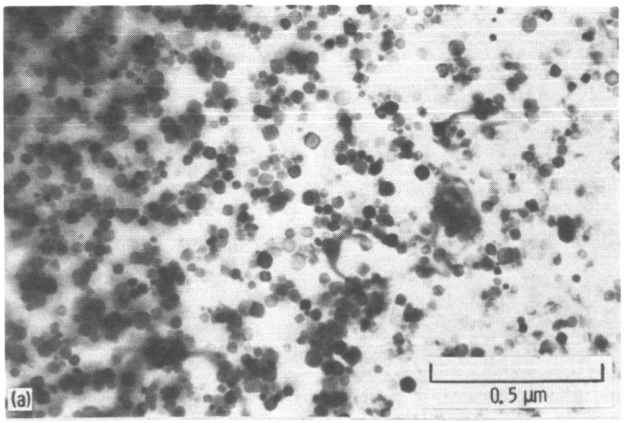

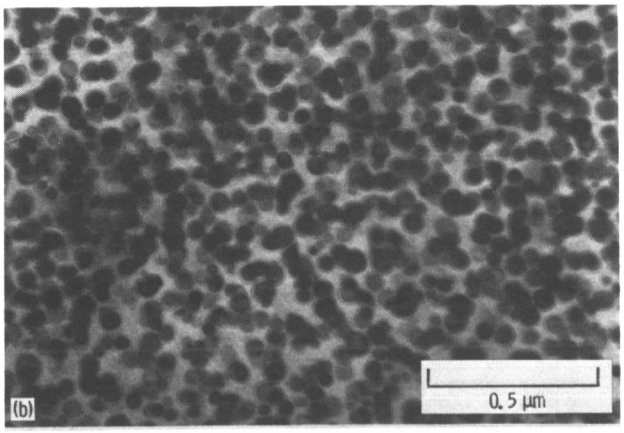

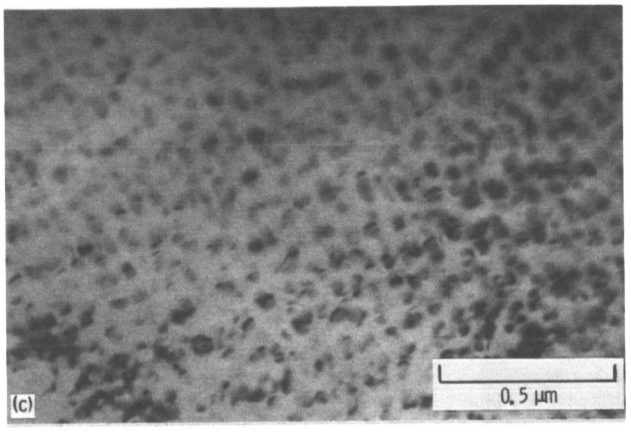

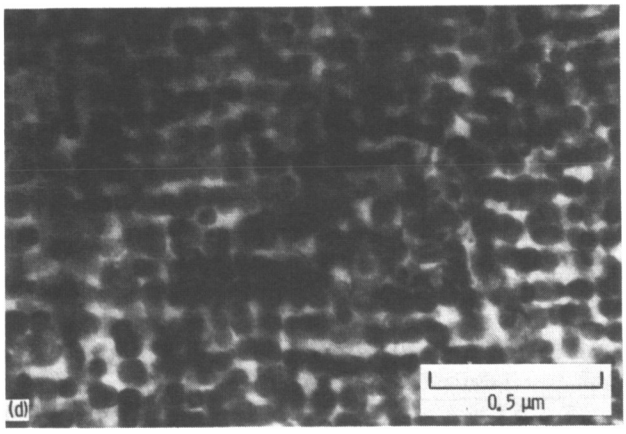

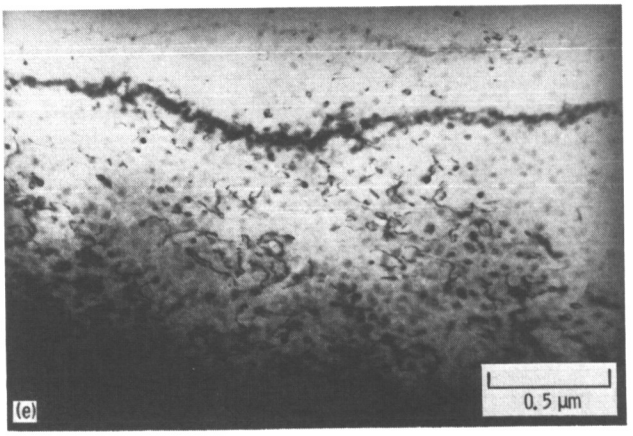

(a) NCG–3 incoherent gamma-prime particles.
(b) NCG–4 incoherent gamma-prime particles.
(c) NCG–5 coherent gamma-prime particles.
(d) NCG–12 coherent gamma-prime particles.
(e) NCG–7 showing pinning of dislocations.

Figure 4.—Representative TEM micrographs of heat-treated alloys.

TABLE III.—MECHANICAL PROPERTY DATA

(a) Yield strength at room temperature

Al, wt %	Cr, wt %			
	12.0	8.0	4.0	0.0
	Yield strength, MPa			
1.5	601	613	616	643
3.0	685	671	700	643
6.0	702	732	799	889

(b) Yield strength at 760 °C

	Yield strength, MPa			
1.5	613	594	583	526
3.0	583	634	640	571
6.0	670	527	583	510

(c) Ultimate tensile strength at room temperature

	Ultimate tensile strength, MPa			
1.5	768	768	792	797
3.0	714	671	759	643
6.0	833	797	799	889

(d) Ultimate tensile strength at 760 °C

	Ultimate tensile strength, MPa			
1.5	639	620	605	541
3.0	619	675	664	585
6.0	721	717	583	539

(e) Stress-rupture life at 172 MPa and 760 °C

	Stress-rupture life, hr			
1.5	402	1343	956	419
3.0	220	161	2600	330
6.0	197	211	0.2	93

(f) Stress-rupture life at 276 MPa and 760 °C

Al, wt %	Cr, wt %			
	12.0	8.0	4.0	0.0
	Stress-rupture life, hr			
1.5	26	36	53	14
3.0	42	29	63	22
6.0	10	11	1.3	2

(g) Elongation during room-temperature tensile testing

	Elongation, percent			
1.5	5.0	4.0	5.0	4.0
3.0	4.0	1.0	4.0	1.0
6.0	4.0	1.0	1.0	1.0

(h) Elongation during 760 °C tensile testing

	Elongation, percent			
1.5	4.0	3.6	4.3	3.6
3.0	4.0	4.0	4.0	2.0
6.0	3.6	4.3	0.0	4.3

(i) Elongation during stress-rupture testing at 760 °C and 172 MPa

	Elongation, percent			
1.5	5.0	5.8	6.5	5.0
3.0	6.5	5.0	7.8	5.0
6.0	7.8	6.0	0.0	7.8

(j) Minimum creep rate at 172 MPa and 760 °C

	Minimum creep rate, sec^{-1}			
1.5	6×10^{-10}	7×10^{-10}	8.5×10^{-9}	5×10^{-10}
3.0	6×10^{-10}	3.5×10^{-9}	6×10^{-10}	6×10^{-9}
6.0	4×10^{-9}	6.5×10^{-9}	---------	8.5×10^{-8}

ultimate tensile strength ranged from 539 MPa for NCG-12 (0 wt % Cr and 6 wt % Al) and NCG-4 (0 wt % Cr and 1.5 wt % Al) to 721 MPa for NCG-9 (12 wt % Cr and 6 wt % Al) (table III(d)). NCG-9 had the lowest Fe content, while NCG-4 had the highest Fe content. An increase in Fe content may lower the strength of alloys because the interatomic spacing is greater between iron atoms than between nickel atoms. The ultimate tensile strength of the alloys increased with increasing Cr at 760 °C (table III(d)). Alloys with 3 wt % Al had a higher ultimate tensile strength than 1.5 wt % Al alloys.

Figure 5 is a plot of the ultimate tensile strength against total Cr and Al content. At room temperature, the ultimate tensile strength remained constant. However, at 760 °C, the ultimate tensile strength increased in proportion to the Cr and Al content. This indicates the significance of solid-solution strengthening at elevated temperatures in this alloy system; at elevated temperature strength increased with increasing substitutional atom (Cr and Al) content.

The percent elongation for room-temperature and 760 °C tensile specimens is shown in tables III(g) and (h).

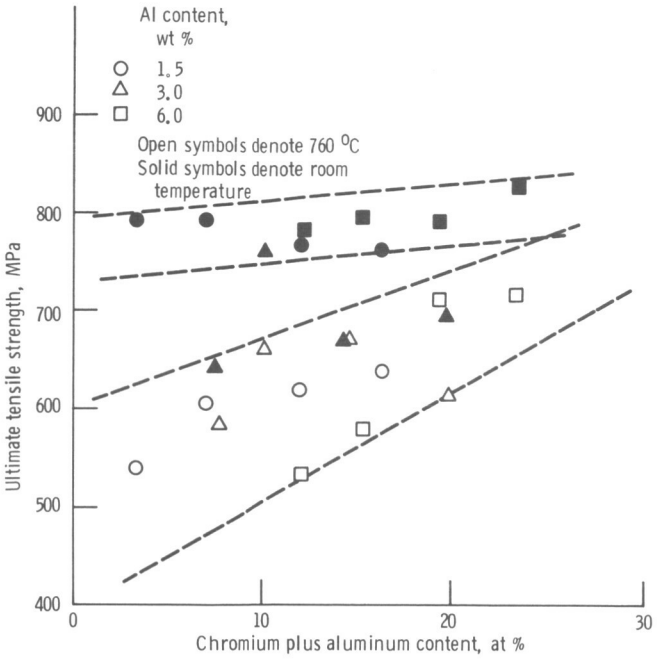

Figure 5.—Effect of total Cr plus Al content on ultimate tensile strength of modified CG-27 alloys.

The tensile elongation at room temperature and at 760 °C was approximately 4 percent for the standard alloy and most of the alloy modifications. Alloys NCG-6, NCG-8, NCG-10, and NCG-12, which contained an acicular beta phase, had about 1 percent elongation at room temperature, while at 760 °C, the effect of the beta phase was negligible, and elongation for these alloys increased appreciably.

Representative tensile fracture surfaces are shown in figure 6 for chromium-free alloys NCG-4, NCG-8, and NCG-12 tested at 760 °C. Both NCG-4 and NCG-8 with 1.5 and 3.0 wt % Al had ductile fractures. At 6.0 wt % Al (NCG-12), the fracture was a mixed-mode fracture with large areas of the fracture surface covered by cleavage fractures (fig. 6(c)).

Stress-rupture.—Stress-rupture lives at 172 MPa are given in table III(e). At 1.5 wt % Al, stress-rupture life increased with increasing Cr up to 8 wt % but fell at 12 wt % Cr. At 3.0 wt % Al, the maximum stress-rupture life occurred at 4 wt % Cr, where NCG-7 reached a stress-rupture life of 2600 hr. This compared to a stress-rupture life of about 402 hr for the standard alloy, NCG-1. The stress-rupture life of alloys with 6.0 wt % Al was uniformly low regardless of the Cr content. The percent elongation of the matrix of alloys generally increased with a reduced strain rate (stress-rupture testing compared with tensile testing). In stress-rupture testing the maximum elongation was 7.8 percent. The minimum creep rate of 6 wt % Al alloys was greater than that of either 1.5 or 3.0 wt % Al alloys for any given Cr content. The highest measured minimum creep rate was 8.5×10^{-8} s^{-1} for NCG-12. The lowest minimum creep rates were from 5×10^{-10} s^{-1} to 6×10^{-10} s^{-1} for NCG-1, NCG-4, NCG-5, and NCG-7.

The stress-rupture lives of the experimental alloys at 276 MPa are given in table III(f). The stress-rupture life of the standard alloy, NCG-1, at 276 MPa was 26 hr. NCG-7 (4 wt % Cr and 3 wt % Al) had the maximum stress-rupture life of 63 hr. All the stress-rupture lives of 6.0 wt % Al alloys were low. For 1.5 and 3.0 wt % Al, the stress-rupture life reached a minimum at 0 wt % Cr. The stress-rupture life reached a maximum at 4 wt % Cr for alloys with 1.5 (NCG-3) and 3.0 wt % (NCG-7) Al. Alloys with 6 wt % Al reached a maximum stress-rupture life of 11 hr at 8 wt % Cr.

Stress-rupture life and minimum creep rate (table III(j)) are plotted against total Cr and Al content in figures 7 to 9. Although the data were scattered, there appeared to be a relationship between stress-rupture life and Cr and Al content, as shown in figures 7 and 8. At a stress of 172 MPa (fig. 7), stress-rupture life increased with increasing Cr and Al content up to a maximum at about 11 at % Cr and Al. As the Cr and Al content increased to greater than 11 at %, the stress-rupture life decreased sharply to a minimum near 20 at % Cr and Al. This trend was more pronounced at 276 MPa, as shown in figure 8. Minimum creep rate cannot be related to Cr and Al content, as shown in figure 9. While the Al content appeared to affect the minimum creep rate, Cr content had little effect. The percent elongation for stress-rupture at 172 MPa and 760 °C is given in table III(j). The elongation of the alloys ranged from 0 to 7.8 percent. This significant increase over the 760 °C tensile elongation (from 0 to 4.3 percent) indicates a degree of strain rate sensitivity.

Representative fracture cross sections are shown in figure 10. Alloys NCG-2, NCG-6, and NCG-10 have 8 wt % Cr and 1.5 wt %, 3.0 wt %, and 6.0 wt % Al. The fractures showed limited ductility; they did not appear to follow any preferred phase. However, preferred oxidation occurred on the surface of NCG-10, as shown in figure 10(d). Under stress this oxidation might open surface cracks leading to failure.

Oxidation

Oxidation rates.—Duplicate specimens of the 12 alloys were tested for 200 1-hr cycles at 870 °C. Weight loss as a function of time is shown in figure 11. The alloys can be divided into three groups based on the shapes of their weight gain curves after 200 cycles: linear, mixed behavior, and parabolic. NCG-3 had linear spalling behavior. Alloys NCG-2, 8 wt % Cr, and NCG-4,

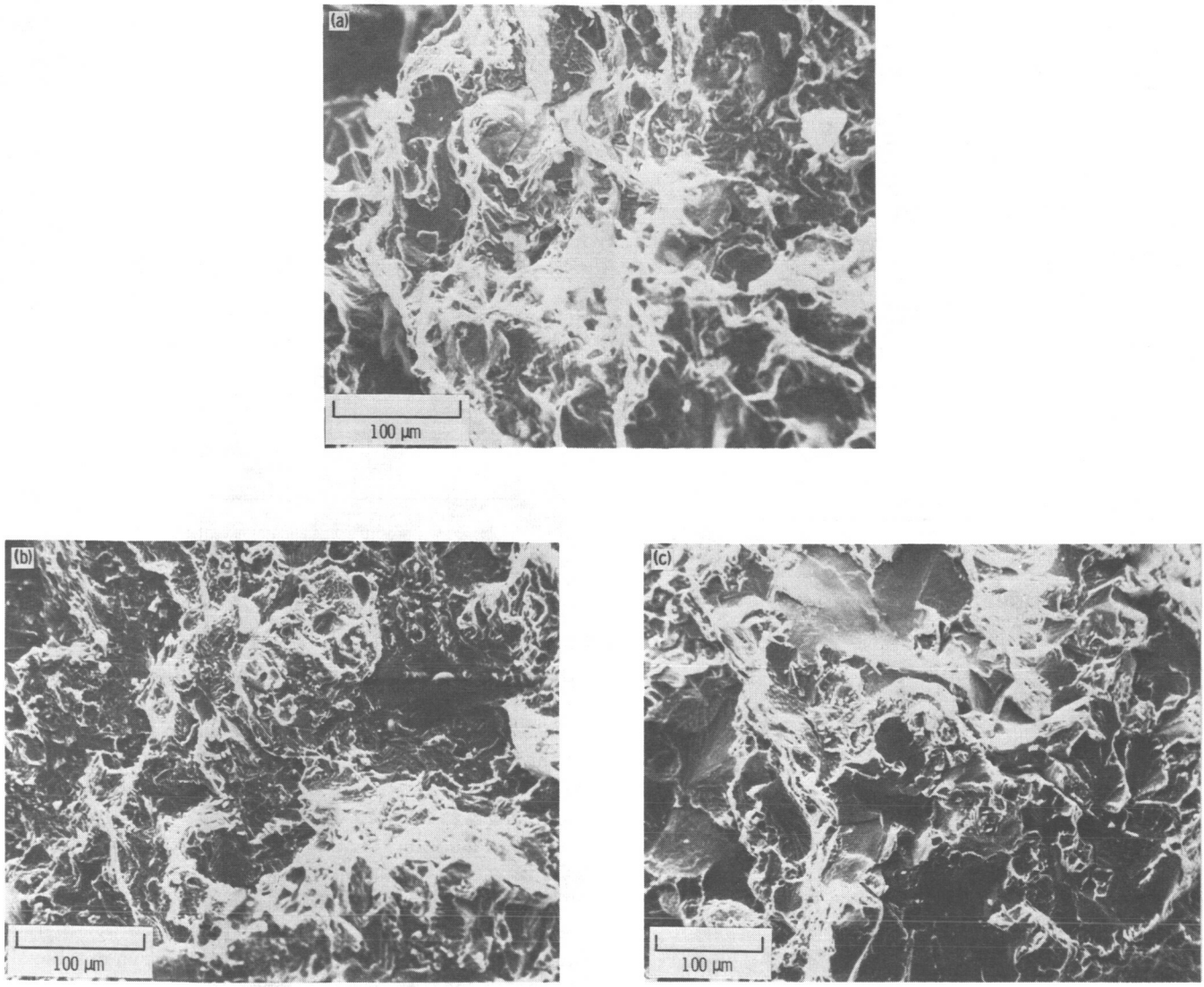

(a) NCG-4.
(b) NCG-8.
(c) NCG-12.

Figure 6.—Representative tensile fracture surfaces for alloys tested at 760 °C.

0 wt % Cr, had mixed behavior. Initially they gained weight, but by 40 cycles spalling exceeded weight gain. NCG-2 and NCG-4 had weight losses between 8 and 12 mg/cm^2. The remaining alloys oxidized parabolically. NCG-5, NCG-6, NCG-8, and NCG-10 gained less weight than NCG-1. This weight gain was in the range 2 to 6 mg/cm^2 after 200 cycles. Three alloys, NCG-7, NCG-9, and NCG-12, gained more weight than NCG-1, the standard alloy. NCG-1 had a weight gain of 10 mg/cm^2. Alloys NCG-7, NCG-9, and NCG-12 had weight gains ranging from 24 to 29 mg/cm^2 after 200 cycles.

When Cr was reduced from 12 wt %, 1.5 wt % Al was not sufficient to preclude rapid spalling. As the Al content was increased to 3 wt %, the level of Cr plus Al was sufficient to provide protection against rapid spalling. At 6 wt % Al, there was a rapid initial growth of an oxide followed by a more moderate weight gain.

The oxidation attack parameter K_a was calculated for each of the 12 alloy modifications. The attack parameter reflects the influence of spalling on the oxidation behavior of the alloy since k_2 is more heavily weighted in the equation $K_a = k_1 + 10k_2$. NCG-3 was fitted to a linear spalling equation, $K_a = 20k_2t$. The calculated oxidation

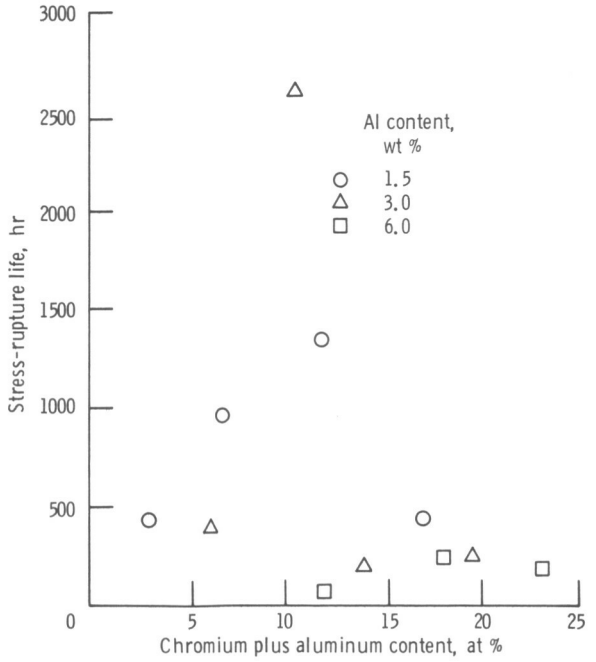

Figure 7.—Effect of total Cr plus Al content on stress-rupture life of modified CG-27 alloys at 760 °C and 172 MPa.

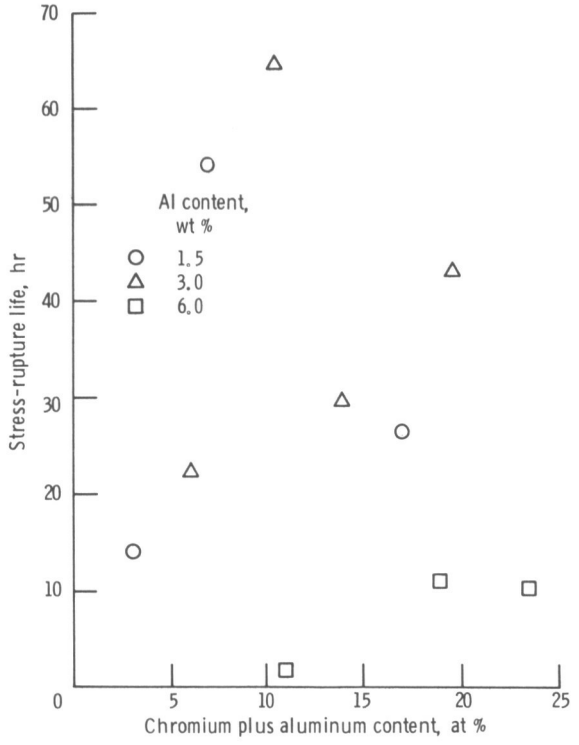

Figure 8.—Effect of total Cr plus Al content on stress-rupture life of modified CG-27 alloys at 760 °C and 276 MPa.

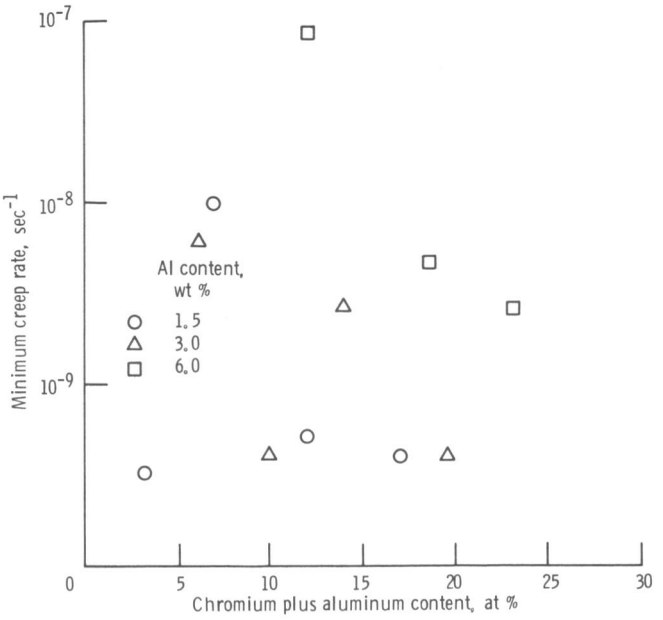

Figure 9.—Effect of total Cr plus Al content on minimum creep rate of modified CG-27 alloys at 760 °C and 172 MPa.

attack parameter was plotted against the Cr and Al content for each alloy (fig. 12 and table IV). For 1.5 and 3.0 wt % Al, the attack parameter was a linear function of the Cr and Al content. Considerable scatter occurred with the 6.0 wt % Al alloys. The oxidation attack parameter was reduced with an increase in Al from 1.5 to 3 wt %. This indicates that 3.0 wt % Al is an optimum level of Al for oxidation resistance. The standard alloy, NCG-1, contains 1.5 wt % Al.

X-ray diffraction.—The postexposure x-ray diffraction data from the specimen surface are shown in table V. In general, the surface oxide consisted of a complex spinel and sesquioxide. The lattice parameter of the spinels ranged from 0.825 to 0.840 nm. The lattice parameter of chromite spinel ranged from 0.835 to 0.840 nm. NCG-4 and NCG-12, which do not contain Cr, had lattice parameters of 0.835 nm, within the range of chromite spinel. These large lattice parameters may be due to the expansion of the lattice by the reactive element Nb. NCG-6, NCG-8, and NCG-10, which had weight gains lower than the standard alloy, NCG-1, had Al_2O_3 in the surface oxide. Two alloys (NCG-7 and NCG-12) which gained weight at a faster rate than NCG-1 contain $NiTiO_3$.

Oxide cross sections.—Oxide cross sections are shown in figures 13 to 15. Oxide morphologies can be divided

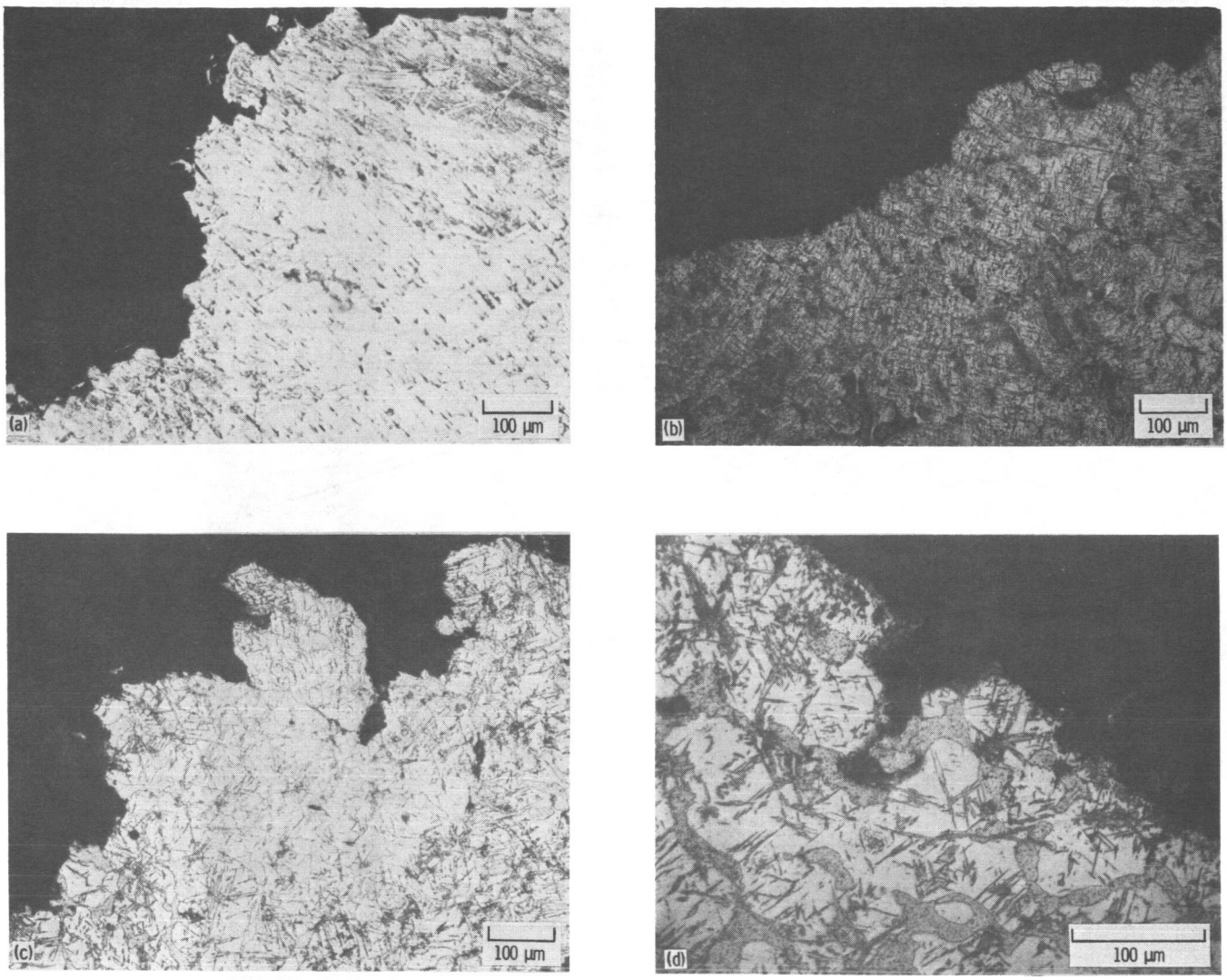

(a) NCG-2.
(b) NCG-6.
(c) NCG-10.
(d) NCG-10.

Figure 10.—Stress-rupture fracture cross sections of modified CG-27 alloys tested at 760 °C and 172 MPa. Tensile bar surface showing oxide penetration of surface.

into three groups. The first group, NCG-1, NCG-5, NCG-6, NCG-7, and NCG-8 developed thin, fine-grained oxides and exhibited parabolic behavior. The second group, NCG-9, NCG-10, and NCG-12, developed thick, fine-grained oxides and exhibited parabolic oxidation behavior. The final group, NCG-2, NCG-3, and NCG-4, developed thick, coarse-grained oxides and had oxidation curves dominated by spalling.

The first group of alloys is characterized by oxide layers of less than 5 μm, as shown in figure 13(a) and (b). In NCG-1 and NCG-7, the oxide consisted of only one layer underlain by a porous oxide-metal boundary. The oxide layer did not follow preferential paths through the grain boundaries.

Energy dispersive x-ray analysis profiles are shown in figure 14 for NCG-7. The oxide-metal interface is shown

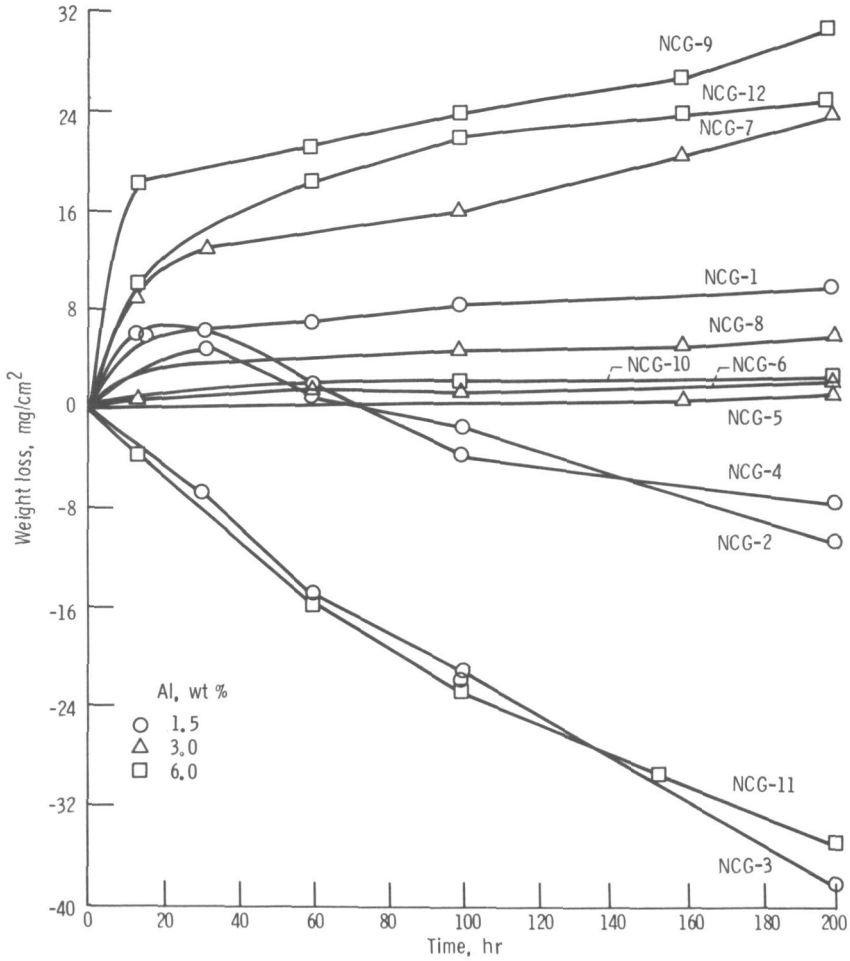

Figure 11.—Cyclic oxidation curves for modified CG-27 alloys at 870 °C for a maximum of 200 1-hr cycles.

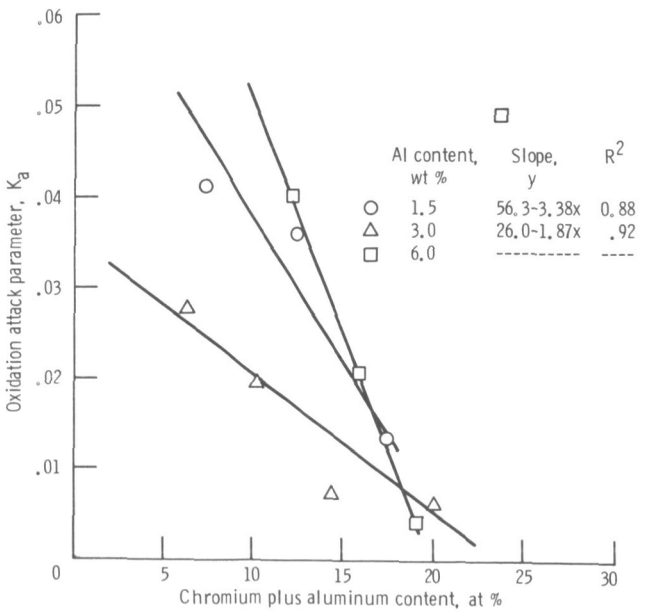

Figure 12.—Effect of total Cr plus Al content on oxidation attack parameter of modified composition CG-27 alloys.

TABLE IV.—OXIDATION ATTACK PARAMETER

Al, wt %	Cr, wt %			
	12.0	8.0	4.0	0.0
	Oxidation attack parameter, K_a			
1.5	0.013	0.035	0.040	0.182
3.0	.006	.007	.019	.027
6.0	.048	.003	.020	.039

in figure 14(a). The interface is somewhat diffuse because of long counting times. As may be seen in figures 14(b) and (d), both Fe and Ni were depleted in the porous oxide-metal interface and in the surface oxide layer. As shown in figure 14(c), Cr was enriched in the outer oxide layer. Aluminum was highly enriched in the layer between the porous zone and the outer oxide layer, as shown in figure 14(e).

The second group of alloys, which had thick oxides and parabolic oxidation can be characterized by NCG-9

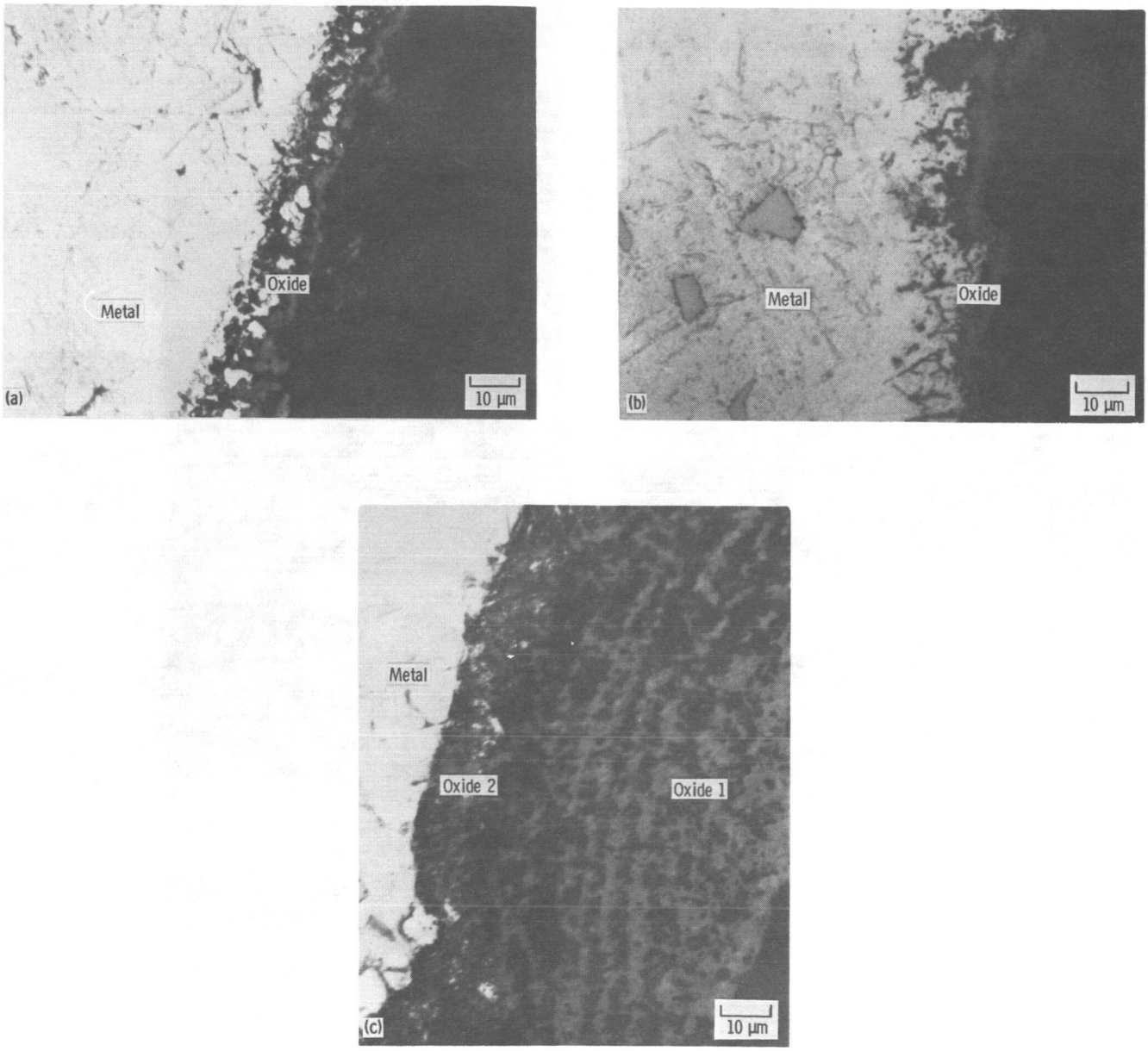

(a) NCG-1.
(b) NCG-7.
(c) NCG-9.

Figure 13.—Optical micrographs of representative oxide cross sections in modified CG-27 alloys.

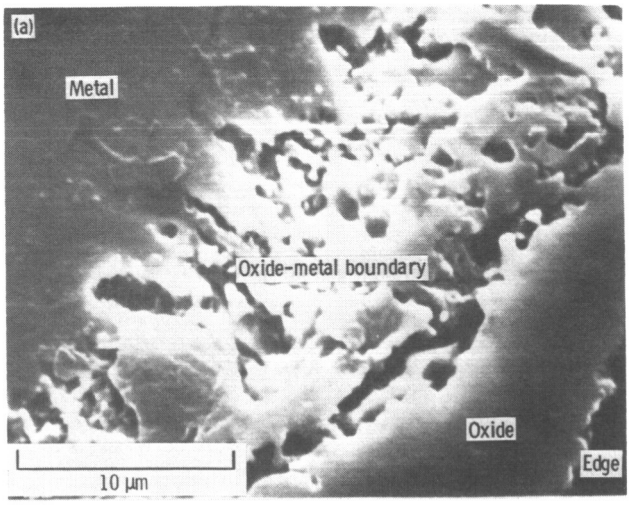

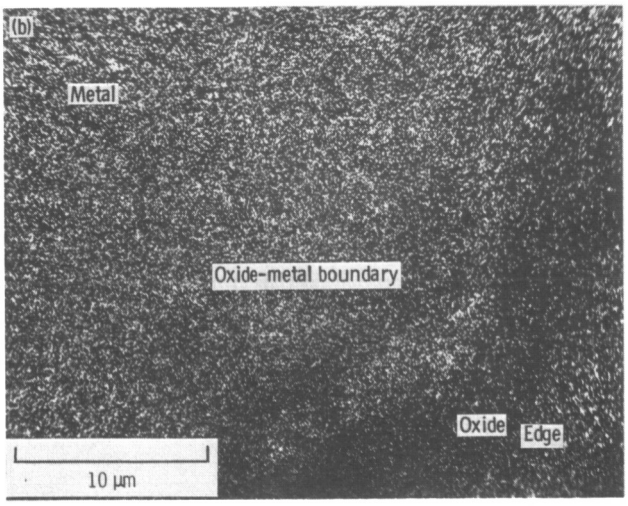

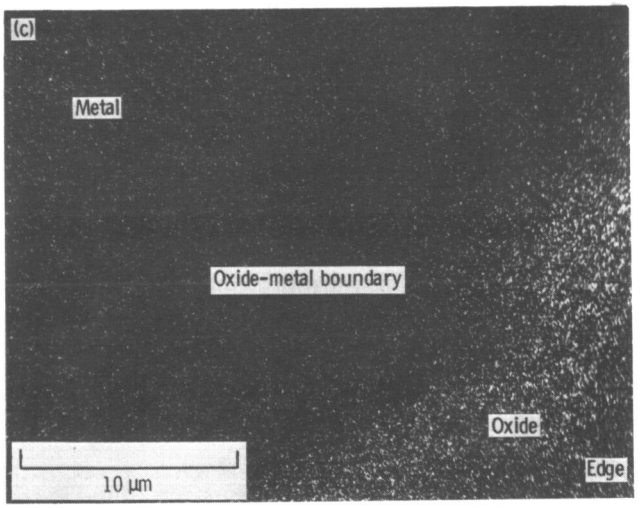

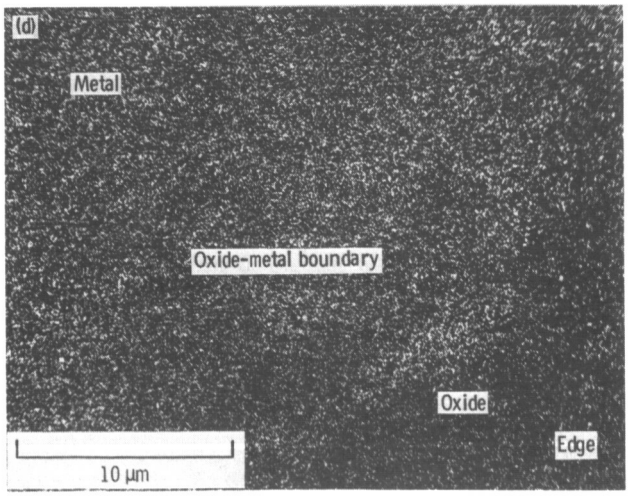

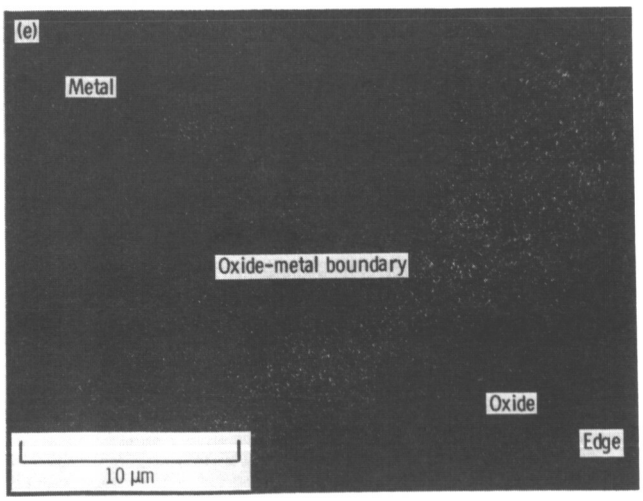

(a) NCG–7. (b) Fe. (c) Cr. (d) Ni. (e) Al.

Figure 14.—SEM and x-ray spectra of modified CG-27 alloy NCG–7.

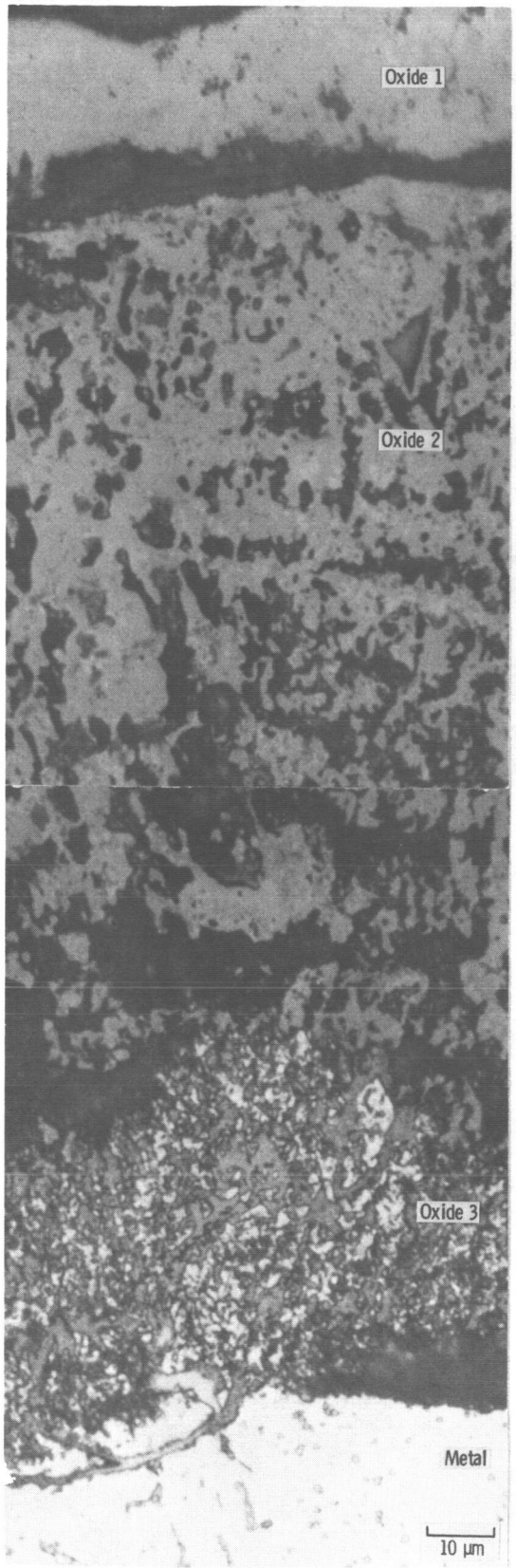

Figure 15.—Optical micrograph of oxide cross section of NCG-3.

TABLE V.—X-RAY DIFFRACTION ANALYSIS OF SPINEL OXIDE PHASES PRESENT ON MODIFIED ALLOYS AFTER EACH CYCLIC OXIDATION AT 870 °C

Alloy	Nominal composition, wt %		Lattice parameter, nm	Oxide phases
	Cr	Al		
NCG-1	12	1.5	0.830	Cr_2O_3
NCG-2	8	1.5	.830	Cr_2O_3
NCG-3	4	1.5	.840	M_2O_3, rutile
NCG-4	0	1.5	.835	Fe_2O_3
NCG-5	12	3.0	.835	Cr_2O_3, rutile
NCG-6	8	3.0	.830	Al_2O_3, Cr_2O_3
NCG-7	4	3.0	.840	$NiTiO_3$, rutile
NCG-8	0	3.0	.825	Al_2O_3, rutile
NCG-9	12	6.0	.835	Fe_2O_3
NCG-10	8	6.0	.825	Cr_2O_3, Al_2O_3, rutile
NCG-11	4	6.0	.835	Fe_2O_3, rutile
NCG-12	0	6.0	.835	$NiTiO_3$

(fig. 13(c)). The oxide which formed on NCG-9 was similar to the oxide formed on NCG-3, as shown in figure 15. The principal difference was that NCG-9 lacked the coarse-grained ferrous surface oxide present in NCG-3. The outermost oxide on NCG-9 was a fine-grained, layered oxide ranging to about 60 μm in thickness. The fine layering corresponded to cyclic oxidation. Layers were separated by porous zones. This indicated that during cooling, the oxide layer separated from the oxide-metal interface but had sufficient strength not to spall. The second major oxide zone, between the layered oxide and the metal, consisted of islands of metal in an oxide matrix. Again there was a uniform boundary between the oxide-metal interface.

The final group of alloys, which exhibited extensive spalling, had a three-layer oxide, as shown in figure 15. The surface oxide layer, approximately 20 μm thick, relatively dense and coarse-grained, was separated from the second oxide layer by a sharp boundary. The second oxide layer, consisting of many zones about 10 μm thick, was fine-grained and highly porous. There was a diffuse boundary between the second and third oxide layers. The third, inner layer consisted of islands of metal surrounded by oxide. The austenitic matrix was preferentially oxidized over the gamma-prime or carbide phases. The interface between the third oxide layer and the metal was smooth, which indicated uniform oxidation.

The distribution of Fe, Cr, and Ni is shown in figure 16 for NCG-3. Chemical differences between the three oxide layers exist. Iron was highly enriched in the outermost oxide layer (fig. 16(b)), present at a lower level

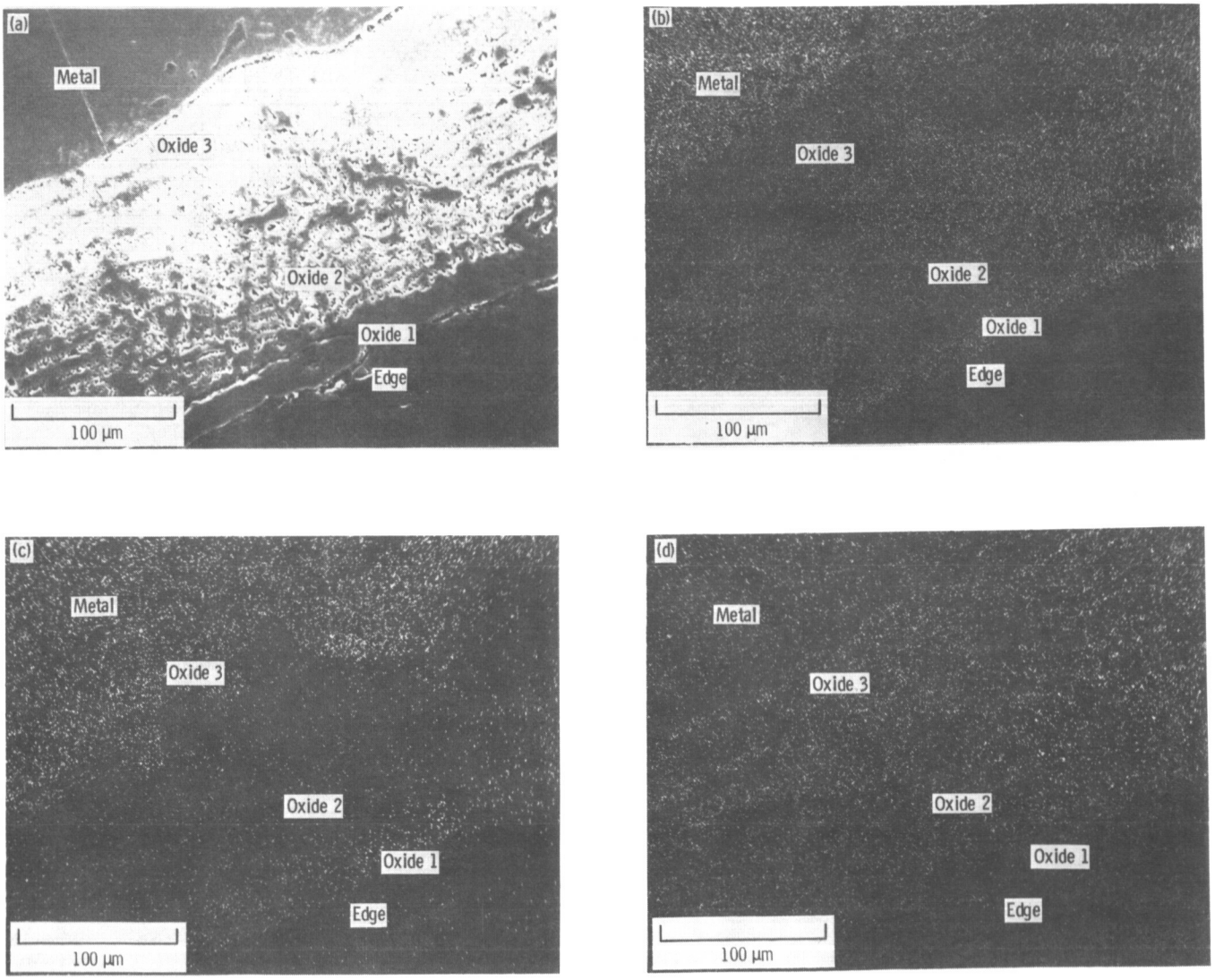

(a) NCG-3. (b) Fe.
(c) Cr. (d) Ni.

Figure 16.—SEM and x-ray spectra of modified CG-27 alloy NCG-3.

in the second oxide layer, and strongly depleted in the third oxide layer near the oxide-metal interface. In contrast, Ni was enriched in both the second and third oxide layers compared with the alloy. Cr was depleted in the second oxide layer except near the interface of the first and second oxide layers. Cr was enriched directly underneath the coarse-grained outside oxide layer and in the internally oxidized third metal-oxide layer, as shown in figure 16(c).

Oxide surfaces.—Representative scanning electron micrographs of oxide surfaces exposed to 200 cycles at 870 °C are shown in figure 17. Alloys which oxidize parabolically are shown in figures 17(a) to (c). These oxide surfaces are characterized by a uniform fine-grained oxide. In general, the oxide grains were approximately 1 μm in diameter. The shapes of the oxide grains ranged from equiaxed to acicular in NCG-7. In contrast, alloys whose oxidation behavior was dominated by spalling had coarse-grained oxides, as shown in figures 17(d) to (f). Oxide grain sizes ranged from 2 μm (fairly fine-grained) in NCG-2 to about 10 μm in NCG-3 and NCG-4. These oxides are characterized by equiaxed grains which were arranged like paving blocks. These surface oxides resulted from recrystallization and grain growth of the second, fine-grained oxide layer. Evidence of recrystallization included skeletal oxide grains, shown in figure 17(d), and mound-shaped coarse-grained oxide formations over a fine-grained substrate, shown in figure 17(e). A region showing spalled and unspalled subregions is shown in figure 17(f). The coarse-grained, unspalled layer had a grain size ranging from about 2 to 10 μm. The spalled layer was composed of fine grains (about 1 μm) arranged in close packing.

The relative intensity of the energy-dispersive spectra from the surface spinels is given in table VI. Except for NCG-9, alloys which exhibited parabolic behavior had reactive metals such as Ti, Al, or Nb in their oxides. Alloys which were dominated by spalling had iron-rich, iron-nickel oxides. In NCG-1, the standard alloy, Cr, Fe, and Ti were the principal elements in the surface oxide. When the Cr content was reduced from 12 wt % (NCG-1) to 8 wt % (NCG-2), Cr no longer appeared in the surface scale. Instead, the predominant element in the outside scale was Fe. The surface beneath the spall was richer in Ni than Fe in contrast to the surface of the spall, which was richer in Fe than Ni. This pattern was repeated in NCG-3 and NCG-4, which were dominated by spalling. The level of aluminum was increased from 1.5 to 3.0 wt % in alloys NCG-5, NCG-6, NCG-7, and NCG-8. The surface oxide on NCG-5 (12 wt % Cr and 3.0 wt % Al) was similar to the surface oxide formed on the standard alloy; however, the reactive elements, Al and Nb, appeared in the oxide. Al and Nb also appeared in NCG-6 (8 wt % Cr) and NCG-7 (4 wt % Cr). As might be expected, Cr decreased in relative value in proportion to the decrease in Cr in the base alloy. Only Fe, Ni, and Nb were present in alloy NCG-8 (0 wt % Cr). With an increase in Al to 6 wt %, there was a decrease in the relative value of Cr compared with alloys containing 3 wt % Al. Reactive elements such as Al, Ti, and Nb were present in NCG-10 and NCG-12. The presence of reactive elements such as Al and Nb apparently controlled the oxide grain growth, which in turn controlled spalling. While the oxide layer on the surface of NCG-9 was thick, it remained fine-grained in contrast to NCG-2, where the outside oxide layer coarsened. The difference between the alloys is an increase in Al from 1.5 to 6 wt %. Internal oxidation of aluminum must also control the oxidation kinetics of chromium; when the chromium content remained constant and the aluminum content was increased, there was a relatively lower amount of chromium spinel in the surface oxide.

Oxide growth.—Three alloys, NCG-1, NCG-3, and NCG-7, were chosen to study the early development of surface oxides by isothermal oxidation tests at 870 °C. These oxides are shown in figures 18 to 20. NCG-1 was chosen as the standard alloy, NCG-3 as an alloy which exhibited spalling, and NCG-7 as an alloy with parabolic oxidation behavior.

After 0.5 hr, fine-grained oxides were formed on NCG-1, NCG-3, and NCG-7. Both NCG-1 and NCG-7 formed a dense surface oxide with a grain size of about 0.5 μm. The oxidation surface had a typical rumpled appearance. In contrast, two oxides formed on the surface of NCG-3. The first oxide formed a flat, porous oxide on the surface of the alloy. The grain size of this alloy was about 0.5 μm. The second oxide formed as euhedral plates perpendicular to the surface of the alloy. While the chemistry of the surface oxides on NCG-1 and NCG-7 after 0.5 hr was similar to that after 200 hr, the surface of NCG-3 was pure iron oxide (spinel and sesquioxide) after 0.5 hr.

TABLE VI.—RELATIVE INTENSITY OF ENERGY-DISPERSIVE SPECTRA FROM SPINELS

Alloy	Oxidation behavior	$K\alpha$ intensity
NCG-1	Parabolic	Cr > Fe > Ti >> Ni
NCG-2	Paralinear	Scale Fe >> Ni under scale Ni > Fe
NCG-3	Spalling	Fe >> Ni
NCG-4	Paralinear	Fe >> Ni
NCG-5	Parabolic	Cr ≅ Fe > Ni > Ti = Al >> Nb
NCG-6	Parabolic	Fe > Cr > Ni ≅ Al > Ti >> Nb
NCG-7	Parabolic	Fe > Ni > Cr > Ti > Al >> Nb
NCG-8	Parabolic	Fe > Ni > Nb
NCG-9	Parabolic	Ni > Fe >> Cr
NCG-10	Parabolic	Fe > Ni > Al > Cr = Ti
NCG-11	Spalling	Fe >> Ni
NCG-12	Paraboilc	Fe > Ni > Al = Ti = Nb

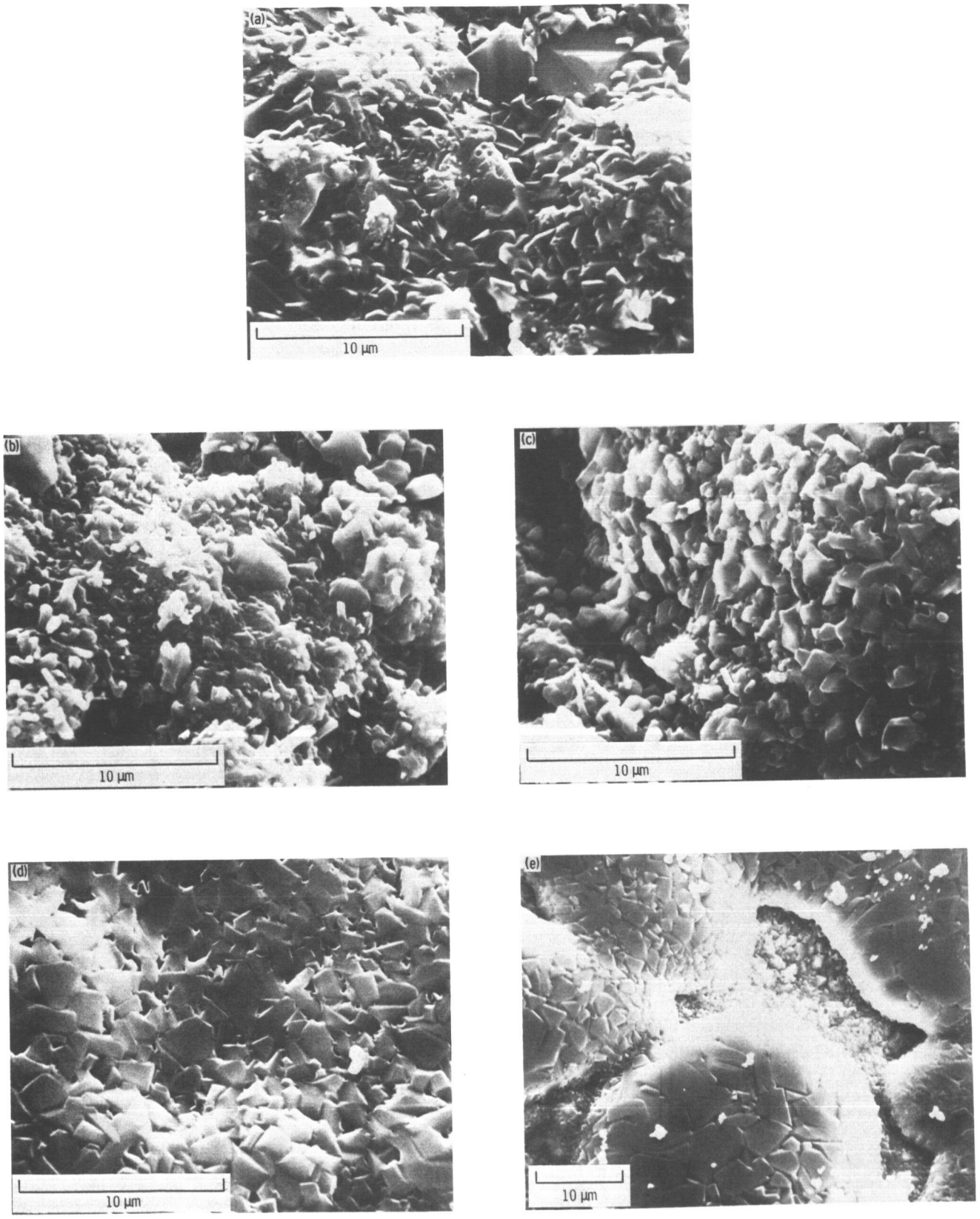

(a) NCG-1. (b) NCG-7. (c) NCG-8. (d) NCG-2. (e) NCG-3.

Figure 17.—SEM micrographs of surface oxides in modified CG-27 alloys after 200 1-hr oxidation cycles at 870 °C.

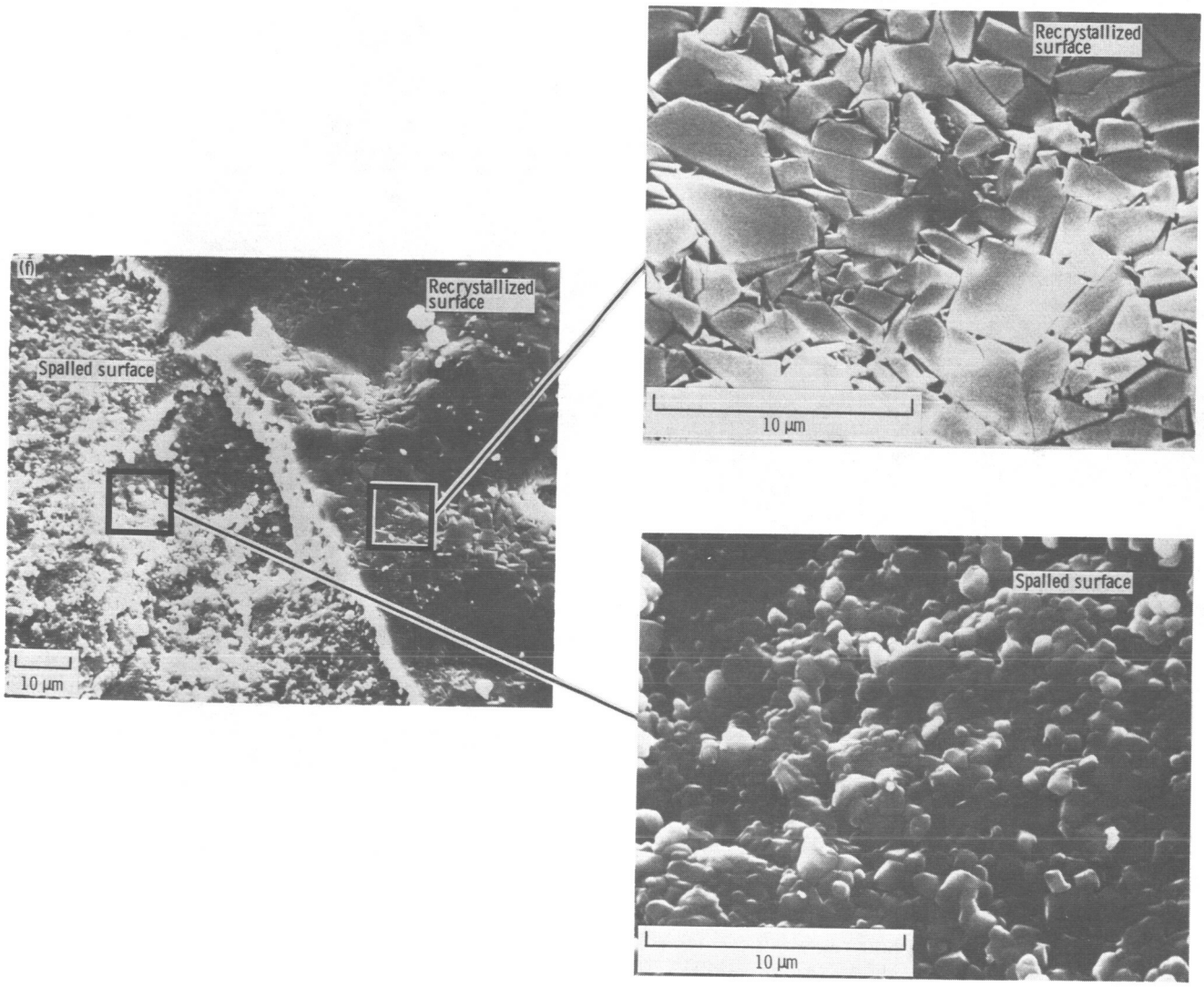

(f) NCG–4 showing coarse-grained, recrystallized oxide and fine-grained, fresh oxide.

Figure 17.—Concluded.

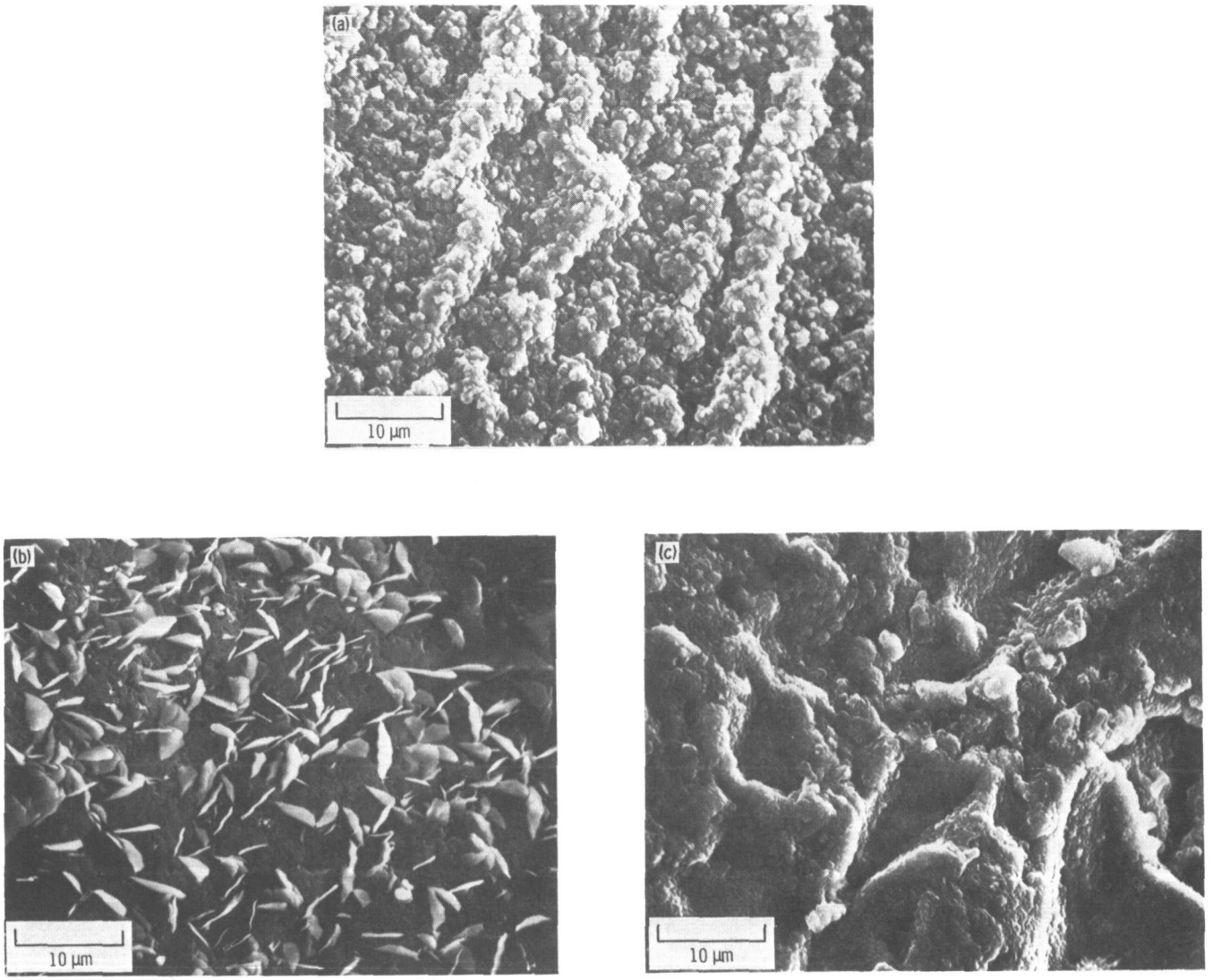

(a) NCG-1. (b) NCG-3. (c) NCG-7.

Figure 18.—SEM micrographs of surface oxides on modified CG-27 alloys after oxidation at 870 °C for 0.5 hr.

NCG-1, NCG-3, and NCG-7 were examined after 20 hr at 870 °C and appeared as shown in figures 19 and 20. The oxide surface of NCG-1 had recrystallized, as may be seen by the difference in the oxide morphology in figures 18(a) and 19(a). There was also a change from a single-phase oxide to a two-phase oxide composed of an equiaxed oxide and an acicular oxide. Similar changes had occurred in NCG-7, although the equiaxed oxide grain size was the same as after 0.5 hr. In contrast, the grain size of NCG-3 had increased dramatically. After 20 hr, the grain size of the equiaxed phase had reached about 3 μm.

The relationship between the original fine-grained oxide and the coarse-grained oxide is shown in figure 20. Grain growth of the outermost oxide layer was probably due to diffusion-induced motion at the grain boundary, where oxygen concentration gradients gave rise to the motion of the boundaries, so that high-diffusivity paths swept through the lattice to aid the transport of oxygen down the gradient. The energy which drove the grain boundaries was the free energy of mixing.

Although this phenomenon has often been observed in metals, it has only recently been observed in an oxide, NiO (ref. 12). The recrystallization observed in NiO at 850 °C was morphologically similar to that of NCG-2, NCG-3, and NCG-4. This recrystallization of the surface oxides on these iron-nickel alloys was only observed when Cr and Al were below a critical level. After 20 hr, iron and nickel oxides were the principal components of NCG-1. Al, Nb, and Cr also appeared in the oxide. In contrast, Fe, Ti, and Cr were the principal components of the surface oxide of NCG-7. Al and Ni also appeared in

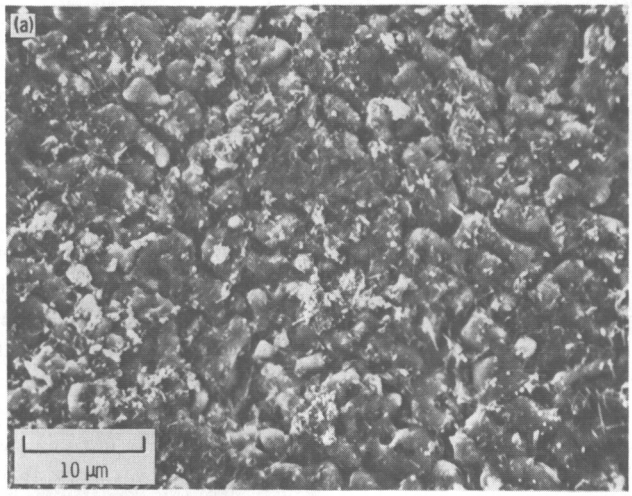

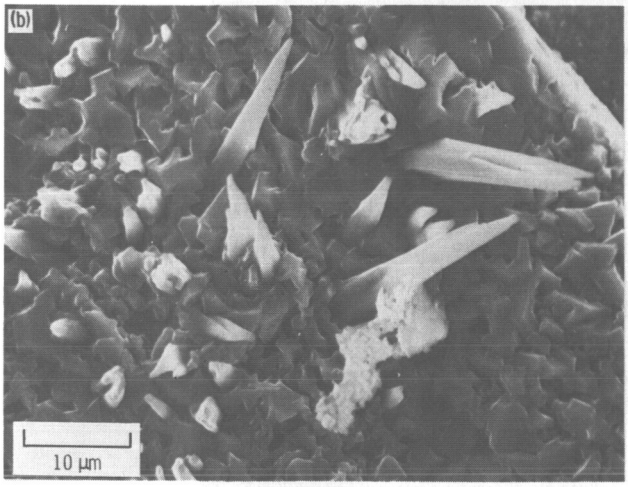

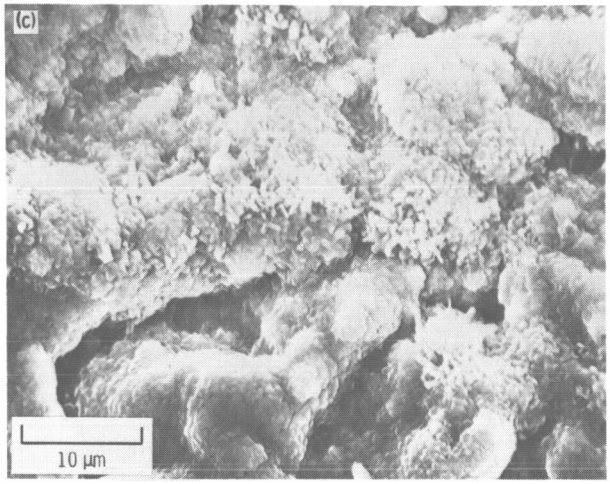

(a) NCG-1. (b) NCG-3. (c) NCG-7.

Figure 19.—SEM micrographs of surface oxides on modified CG-27 alloys after oxidation at 870 °C for 20 hr.

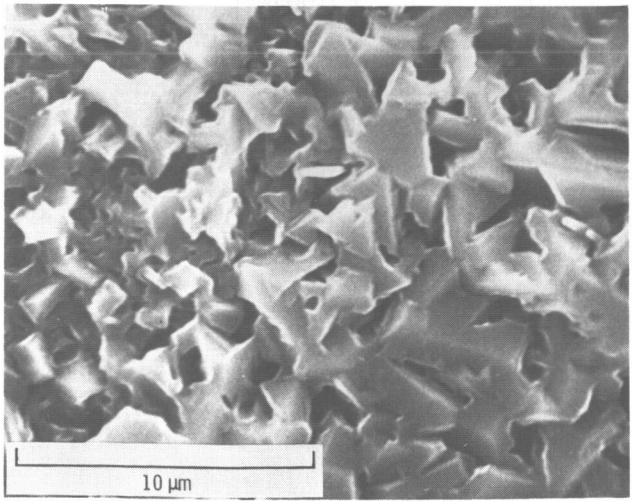

Figure 20.—SEM micrograph of partially recrystallized oxide on NCG-3 (4 wt % Cr and 1.5 wt % Al). Oxidation at 870 °C for 20 hr.

the surface oxide of NCG-7. After 0.5 hr, Fe was the only component of the surface oxide on NCG-3. While Fe was still the major component after 20 hr, Cr, Mo, Ti, and Ni appeared in the surface oxide.

Comparison of Alloy Modifications With Commercial Alloys

A comparison of modified alloys with commercial alloys is shown in figures 21 and 22. Initially CG-27 was chosen for study because of its good mechanical and oxidation properties as well as its low strategic material content (refs. 3 and 13). CG-27 has a chromium content lower than many commercial alloys, including IN800, A286, N155, 19-9DL, and 316SS. Also, CG-27 does not contain Co. The alloy matrix was chosen in order to determine if it would be possible to further reduce the chromium content of CG-27 and still maintain

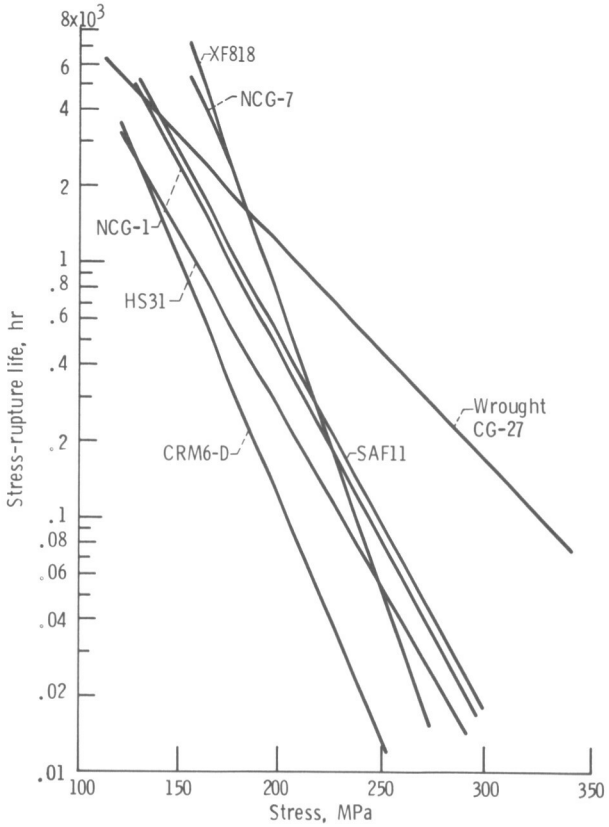

Figure 21.—Stress-rupture life as a function of stress for NCG-7 and commercial alloys.

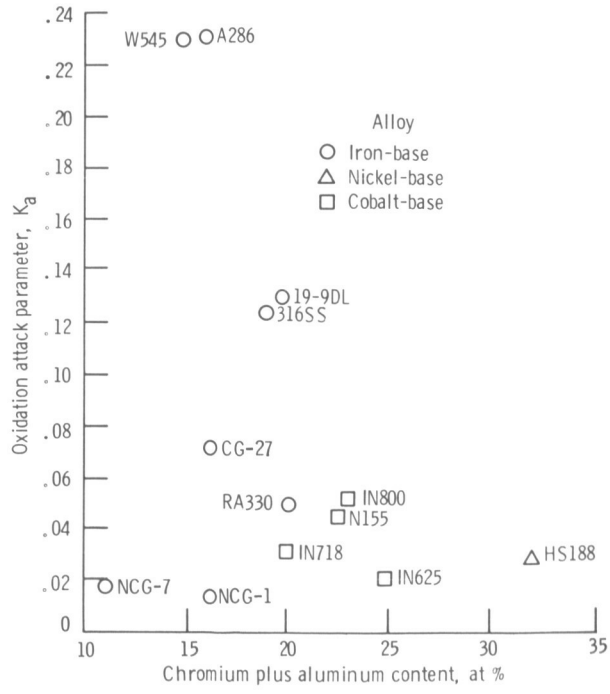

Figure 22.—Effect of total Cr plus Al content on oxidation attack parameter K_a.

mechanical and oxidation properties comparable with the original alloy.

Figure 21 shows the stress-rupture life as a function of stress for NCG-1, NCG-7, and commercial alloys. The data for the commercial alloys were obtained from Titran (ref. 14). The modified alloys had stress-rupture properties comparable with cast carbide-strengthened alloys such as XF818 and SAF11, but are stronger than CRM6D and HS31. The reduced Cr alloy, NCG-7, had stress-rupture properties improved over the standard 12 wt % Cr alloy. In general, wrought alloys have lower slopes than cast alloys. This accounts for the greater stress-rupture life of the commercial wrought CG-27 at higher loads.

Figure 22 shows the oxidation attack parameter of NCG-1, NCG-7, and commercial alloys as a function of total Cr and Al content. The attack parameters for commercial alloys were obtained from Stephens and Barrett (ref. 15). The modified alloys NCG-1 and NCG-7 had lower oxidation attack parameters than the commercial alloys, including CG-27. This may have been due in part to zirconia contamination from the mold. Although NCG-7 had 67 percent less Cr than NCG-1, its attack parameter was similar.

In general, NCG-7 (4 wt % Cr and 3 wt % Al) is a promising alloy for further study. The stress-rupture properties of NCG-7 are somewhat better than those of the standard alloy NCG-1 (cast CG-27). In addition, the increase in Al over wrought CG-27 led to a lower attack parameter than CG-27 or many other commercial alloys.

Concluding Remarks

Although several cast alloys identified by this study have potential for further study based on either mechanical properties or oxidation behavior, the alloy with 4 wt % Cr and 3 wt % Al (NCG-7) combines better stress-rupture properties than the standard alloy (12 wt % Cr and 1.5 wt % Al) and better parabolic oxidation behavior. Based on the results, small additions of Al can be used to lower the level of Cr in iron-nickel-base superalloys without seriously reducing either the mechanical or oxidation properties of the alloys.

Summary of Results

A matrix of alloy modifications based on CG-27, an intermediate-temperature iron-base superalloy, was designed to study the effects of Cr and Al levels. The major results were the following:

Mechanical Properties

1. Alloy NCG-7 (4 wt % Cr and 3 wt % Al) had a stress-rupture life greater than the standard alloy, NCG-1, at 172 and 276 MPa at 760 °C and was comparable with commercial alloys with much higher Cr contents.

2. Additions of up to 3 wt % (6 at %) Al were possible without a reduction in stress-rupture life. Alloys with 6 wt % Al had severely reduced stress-rupture properties. Stress-rupture life also depended on the total Cr and Al content.

3. Dispersion strengthening was the principal role of gamma prime, since loss of coherency could occur without loss of strength.

Oxidation

1. Alloy NCG-7 (4 wt % Cr and 3 wt % Al) had a lower oxidation attack parameter than comparable iron-nickel-base alloys, including A286, 19-9DL, 316SS, and IN800. The oxidation attack parameter was inversely proportional to total Cr and Al content for 1.5 and 3.0 wt % Al alloys.

2. Oxide grain size, which was controlled by Cr and Al, determined spalling. The oxidation curves of alloys with less than 12 wt % Cr and 1.5 wt % Al, whose oxides recrystallized to a very coarse grain size, had large oxide spalling constants. Curves of alloys with 6 wt % Al, which had similar oxide thicknesses but remained fine-grained, were essentially parabolic. Grain growth was due to diffusion-induced recrystallization.

3. Chromium segregated to the surface oxide layer in alloys with parabolic oxidation behavior, such as alloys NCG-1 (12 wt % Cr and 1.5 wt % Al) and NCG-7 (4 wt % Cr and 3 wt % Al). Chromium was concentrated in the second oxide layer of alloys with linear oxidation behavior, such as NCG-2 and NCG-3. Although there was an increase in the relative proportion of Cr in the surface oxide with increasing Cr, an increase in the Al content from 3.0 to 6.0 wt % caused a reduction in the relative proportion of Cr in the surface oxide and a reduction in grain growth. Except for NCG-9 (12 wt % Cr and 6 wt % Al), alloys which exhibited parabolic oxidation had reactive elements such as Ti, Al, or Nb in their oxides.

National Aeronautics and Space Administration
Lewis Research Center
Cleveland, Ohio 44135, November 21, 1984

References

1. Stephens, Joseph R.: A Status Review of NASA's COSAM (Conservation Of Strategic Aerospace Materials) Program. NASA TM-82852, 1982.
2. Simmons, Ward F.; and Wagner Herbert J.: Where You Can Use Today's Superalloys. Met. Prog., vol. 91, no. 6, June 1967, pp. 87-92.
3. Misencik, John A.: Evaluation of CO_2 and CO Dopants in Hydrogen to Reduce Hydrogen Permeation in the Stirling Engine Heater Head Tube Alloy CG-27. NASA TM-83535, 1983.
4. Barrett, C.A.; and Lowell, C.E.: High Temperature Cyclic Oxidation Furnace Testing at NASA Lewis Research Center. J. Test. Eval., vol. 10, no. 6, Nov. 1982, pp. 273-278.
5. Lillys, P., et al.: Hot Strength Iron Base Alloys, US Patent No. 3243287, March 29, 1966.
6. Sullivan, C.P.; and Donachie M.J.: Microstructures and Mechanical Properties of Iron-Base-Containing Superalloys. Met. Eng. Q., vol. 11, Nov. 1971, pp. 1-11.
7. Whitney, C.R.; and Krauss G.: Effects of Titanium and Aluminum Variations on an Iron-Nickel Superalloy. Met. Eng. Q., vol. 11, Nov. 1971, pp. 25-30.
8. Hammond, C.M.; and Ansell G.S.: Gamma-Prime Precipitation in an Fe-Ni Base Alloy. ASM Trans. Q., vol. 57, Sept. 1964, pp. 727-738.
9. Pitler, R.K.; and Ansell G.S.: Precipitation in a High-Nickel Maraging Steel. ASM Trans. Q., vol. 57, no. 1, Mar. 1964, pp. 220-246.
10. Maniar, G.N.; and James H.M.: Electron Microstructure Study of an Iron-Nickel-Base Heat-Resistant Alloy Containing Cobalt. ASTM-STP-430, 1968, pp. 262-272.
11. Kuhlmann-Wilsdorf, Doris: On the Origin of Dislocations. Philos. Mag., vol. 3, no. 26, Feb. 1958, pp. 125-139.
12. Parthasarathy, T.A.; and Shewmon P.G.: Diffusion Induced Recrystallization of NiO. Acta Metall. vol. 32, no. 1, Jan. 1984, pp. 29-33.
13. Misencik, John A.: Evaluation of Candidate Stirling Engine Heater Tube Alloys for 1000 Hours at 760 °C. NASA TM-81578, 1980.
14. Titran, Robert H.: Creep-Rupture Behavior of Candidate Stirling Engine Alloys After Long-Term Aging at 760 °C in Low Pressure Hydrogen. NASA TM-83676, 1984.
15. Stephens, Joseph R. and Barrett, Charles A.: Oxidation and Corrosion Resistance of Candidate Stirling Engine Heater-Head-Tube Alloys. NASA TM-83609, 1984.

1. Report No.	2. Government Accession No.	3. Recipient's Catalog No.
NASA TP-2443		

4. Title and Subtitle	5. Report Date
Effects of Chromium and Aluminum on Mechanical and Oxidation Properties of Iron-Nickel-Base Superalloys Based on CG-27	March 1985
	6. Performing Organization Code: 505-33-62
7. Author(s): Susan R. Schuon	8. Performing Organization Report No.: E-2320
	10. Work Unit No.
9. Performing Organization Name and Address: National Aeronautics and Space Administration, Lewis Research Center, Cleveland, Ohio 44135	11. Contract or Grant No.
	13. Type of Report and Period Covered: Technical Paper
12. Sponsoring Agency Name and Address: National Aeronautics and Space Administration, Washington, D.C. 20546	14. Sponsoring Agency Code

15. Supplementary Notes

Presented in part at TMS-AIME Fall Meeting, Detroit, MI, Sept. 17-20, 1984.

16. Abstract

The effects of chromium and aluminum on the mechanical and oxidation properties of a series of gamma-prime-strengthened alloys based on CG-27 were studied as part of the NASA Conservation of Strategic Aerospace Materials Program. The matrix of the alloys was based on the reduction of Cr from 12 to 8 to 4 to 0 wt %. Aluminum was increased from 1.5 to 3 to 6 wt %. Alloys were tested in tension at room temperature and 760 °C and stress-rupture tested at 760 °C under stresses of 172 and 276 MPa. Alloys were oxidized for 200 1-hr cycles at 870 °C. A reduction in Cr to 4 wt % was possible in this system when the Al content was increased from the nominal 1.5 wt % in CG-27 to 3 wt %. This determination was based on the following results: The stress-rupture life of the alloys reached a maximum at 4 wt % Cr and 3 wt % Al and then dropped at higher levels of Cr and Al. Since gamma-prime coherence had little effect on strength, gamma-prime dispersion and solid-solution strengthening were the principal modes of alloy strengthening. The oxidation attack parameter K_a decreased with increasing Cr and Al contents for each alloy group based on Al content. As a group, alloys with 3 wt % Al had the lowest attack parameters. Therefore, 3 wt % is the optimum level of Al for parabolic oxidation behavior. Spalling, due to diffusion-induced grain growth, was controlled by the overall Cr and Al levels. The alloy with 4 wt % Cr and 3 wt % Al had stress-rupture properties superior to those of the base alloy, CG-27, and maintained parabolic oxidation behavior while the Cr content was reduced by two-thirds of its value in cast CG-27.

17. Key Words (Suggested by Author(s))

Iron alloys
Oxidation
Mechanical properties
Gamma prime

18. Distribution Statement

Unclassified - unlimited
STAR Category 26

19. Security Classif. (of this report)	20. Security Classif. (of this page)	21. No. of pages	22. Price*
Unclassified	Unclassified	24	A02

*For sale by the National Technical Information Service, Springfield, Virginia 2216[illegible]

NASA-Langley, 1985

2 2 1U,C, 850322 S00161DS
DEPT OF THE AIR FORCE
ARNOLD ENG DEVELOPMENT CENTER(AFSC)
ATTN: LIBRARY/DOCUMENTS
ARNOLD AF STA TN 37389